

Theory of superconducting proximity effect in hole-based hybrid semiconductor-superconductor devices

D. Michel Pino,¹ Rubén Seoane-Souto,¹ Maria José Calderón,¹ Ramón Aguado,^{1,*} and José Carlos Abadillo-Uriel^{1,†}

¹*Instituto de Ciencia de Materiales de Madrid (ICMM),
Consejo Superior de Investigaciones Científicas (CSIC),
Sor Juana Inés de la Cruz 3, 28049 Madrid, Spain*

Hybrid superconductor-semiconductor systems have received a great deal of attention in the last few years because of their potential for quantum engineering, including novel qubits and topological devices. The proximity effect, the process by which the semiconductor inherits superconducting correlations, is an essential physical mechanism of such hybrids. Recent experiments have demonstrated the proximity effect in hole-based semiconductors, but, in contrast to electrons, the precise mechanism by which the hole bands acquire superconducting correlations remains an open question. In addition, hole spins exhibit a complex strong spin-orbit interaction, with largely anisotropic responses to electric and magnetic fields, further motivating the importance of understanding the interplay between such effects and the proximity effect. In this work, we analyze this physics with focus on germanium-based two-dimensional gases. Specifically, we develop an effective theory supported by full numerics, allowing us to extract various analytical expressions and predict different types of superconducting correlations including non-standard forms of singlet and triplet pairing mechanisms with non-trivial momentum dependence; as well as different Zeeman and Rashba spin-orbit contributions. This, together with their precise dependence on electric and magnetic fields, allows us to make specific experimental predictions, including the emergence of f-type superconductivity, Bogoliubov Fermi surfaces, and gapless regimes caused by large in-plane magnetic fields.

I. INTRODUCTION

In recent years, superconductor-semiconductor hybrid devices are becoming an exciting playground for exploring new physical phenomena, such as Majorana-based topological protected phases [1–7] and novel qubit designs [8, 9]. The latter, in particular, are becoming an interesting alternative to more traditional qubits due to the benefits arising from the combination of semiconductor and superconductor properties. On the one hand, semiconducting spin qubits [10] are often highly localized, hence potentially more scalable. The natural mechanism for mediating two-qubit gates is the exchange interaction [11–14], which is fast yet quite short-ranged, making it difficult to entangle distant qubits. Superconducting qubits, on the other hand, are easy to couple and read-out by using circuit quantum electrodynamics (cQED) techniques [15], but physically they are much larger, hence potentially less scalable and more susceptible to crosstalk and noise.

To date, the majority of experiments with hybrids have been performed in semiconductors from group III-V materials, such as InAs and InSb, proximitized by a superconductor. In such semiconductors, nuclear spins are unavoidable, resulting in very short coherence times, as recently demonstrated superconducting in spin qubits [16, 17] based on Andreev levels [18–22]. This has recently led to a shift towards group IV semiconductors,

particularly germanium, which naturally comprises over 92% nuclear spinless isotopes and can be isotopically purified to significantly reduce hyperfine noise. Besides, many metals have a Fermi-level pinning to the valence band of Ge [23], making Ge an interesting candidate for the proximity effect on holes. Importantly, holes in the valence band of Ge exhibit a large spin-orbit interaction (SOI), which is a key ingredient in topological superconductivity. Hole bands have a p-orbital character, which together with the spin, leads to total angular momentum $J = 3/2$. The SOI in the valence band manifests in different forms, the predominant term being a cubic in momentum Rashba interaction [24], with small interface-mediated linear corrections [25–27], as well as anisotropic and inhomogeneous g-tensors [28–36]. These mechanisms enable all-electrical manipulation of the spin [37, 38] and strong coupling to photons in superconducting cQED setups [39–43].

Even though the use of Ge for hybrid devices is quite recent, several important achievements have already been demonstrated, including hard-gap superconductivity [44]; gate-tunable transmon (gatemon) qubits [45, 46]; parity-conserving Cooper-pair transport and ideal superconducting diode effect in planar germanium [47, 48]; as well as readout of Andreev levels, using both cQED in planar Ge Josephson junctions [49] and transport spectroscopy in quantum dots [50].

Despite these early successes from the experimental front, the theoretical understanding of the proximity effect in Ge-based hybrids is quite limited. Similarly to the usual procedure with electron states, the simplest route is to add a constant superconductor pairing term to the

* ramon.aguado@csic.es

† jc.abadillo.uriel@csic.es

effective lowest-hole-band theory [51, 52]. The same approach can be extended to assume constant pairings in both heavy and light-hole bands, yielding new effects, such as the renormalization of the hole g-factors [53]. Both models capture part of the hole physics but miss the interplay of the different bands in the superconducting pairing and, hence, a relevant piece of the physics of the device. In fact, based on symmetry, it has been argued that superconducting correlations may only be induced directly to the conduction band [54], perturbatively exporting superconductivity to the valence band. Real devices, however, have interfaces and disorder that break symmetries in all directions, hence, such symmetry arguments are not expected to hold to their full extent.

In this work, we follow a more agnostic route and, starting from a full $8 \times 8 \mathbf{k} \cdot \mathbf{p}$ (8KP) Kane model, derive the possible superconducting pairing terms arising from direct coupling between the superconductor and the distinct conduction and hole bands. From there, we extract the effective theory of hole states in strained Ge devices with vertical confinement that applies to most experimental situations with two-dimensional hole gases (2DHG). Importantly, by considering all the different bands, we find that the pairing terms are rather involved, going beyond s-type superconductivity by including non-trivial k-dependencies coupling the different bands and terms originated from the cubic Rashba contributions. In this context, one of the main results of our work is the derivation of the general structure of a pairing matrix in Eq. (8), where we present in a compact form the effective superconducting pairings of a proximitized 2DHG modelled with a 4-band Kohn-Luttinger Hamiltonian without further approximations. Such form allows to obtain full analytical expressions for pairings in the hole sector containing both singlet and triplet components in the Rashba basis, Eq. (9), by considering that either the conduction, Eq. (10), or the valence band, Eq. (11), are proximitized by a superconductor. Furthermore, our theory includes Zeeman terms and consider orbital corrections, going well-beyond prior theoretical studies on the proximity effect in Ge hybrid devices.

Armed with these results, we discuss various experimental consequences of the proximity effect in a 2DHG in the presence of an external magnetic field. Specifically, we focus on the magnetic field dependence of the density of states (DOS), a quantity directly relevant for tunneling spectroscopy experiments. Our main result here is the emergence of several magnetic-field-dependent logarithmic van Hove singularities, replacing the standard BCS-like square-root singularities (Fig. 7). This behavior is directly linked to the nontrivial properties of the Bogoliubov de Gennes bands in the hole sector (specifically, the distance between the band extrema and the Fermi level has an oscillatory behavior in terms of the in-plane angle of the momentum, (Fig 8). At large in-plane magnetic fields, the proximitized 2DHG becomes gapless and Bogoliubov Fermi surfaces emerge (Fig. 9), a behav-

ior that has recently been observed in a two-dimensional Al-InAs hybrid heterostructure [55] and in a proximitized topological insulator film (bismuth telluride placed on top of superconducting niobium diselenide) [56], see also [57, 58]. Importantly, the intricate form of the proximity effect in the 2DHG results in qualitative differences with respect to a 2DEG, notably various features originating from the gap anisotropy.

The remainder of this paper is organized as follows. In Sec. II, we show the 8KP Ge bulk model in the Bogoliubov-deGennes formalism with pairing terms coming from the conduction band as the starting point of our theory. In Sec. III, we derive the resulting 4KP theory for proximitized hole bands after integrating out the conduction band. These results are used in Sec. IV to extract an effective model for proximitized 2DHG, from which we obtain analytical expressions for the different superconducting pairing terms (Eq. (8)) with contributions from the conduction (Eq. (10)) and valence bands (Eq. (11)). In Sec. V, we discuss different experimental signatures, such as the role of magnetic fields in the gaps including anisotropic g-factors in Subsec. V A. In Subsec. V B, we apply our theory to calculate the magnetic field dependence of the DOS and discuss its various features in terms of the anisotropy of the BdG bands, including the emergence of Bogoliubov Fermi surfaces at large in-plane magnetic fields. Finally, we finish the paper in Sec. VI with a summary of our main results. We have tried to leave in the main text only the most important derivations, trying at all times to lighten the technical burden and reduce the number of equations for the most part to the minimum necessary, and moved all the more dense mathematical developments to Appendices.

II. FULL BDG 8KP MODEL

We first consider an 8×8 Kane model, which in Bogoliubov de Gennes (BdG) formalism can be written as a 16×16 Hamiltonian

$$H = \frac{1}{2} \Psi^\dagger H_{8KP}^{\text{BdG}} \Psi, \quad (1)$$

expressed in terms of a Nambu spinor basis $\Psi = (c_{1/2, \mathbf{k}}, c_{-1/2, \mathbf{k}}, b_{3/2, 3/2, \mathbf{k}}, b_{3/2, 1/2, \mathbf{k}}, b_{3/2, -1/2, \mathbf{k}}, b_{3/2, -3/2, \mathbf{k}}, b_{1/2, 1/2, \mathbf{k}}, b_{1/2, -1/2, \mathbf{k}}, c_{1/2, -\mathbf{k}}, c_{-1/2, -\mathbf{k}}, b_{3/2, 3/2, -\mathbf{k}}, b_{3/2, 1/2, -\mathbf{k}}, b_{3/2, -1/2, -\mathbf{k}}, b_{3/2, -3/2, -\mathbf{k}}, b_{1/2, 1/2, -\mathbf{k}}, b_{1/2, -1/2, -\mathbf{k}})^T$, where $c_{s_z, \mathbf{k}}$ ($b_{j, j_z \mathbf{k}}$) destroys an electron (hole) with angular momentum j , spin projection s_z (angular momentum projection j_z), and momentum \mathbf{k} . For a given chemical potential μ , the BdG Hamiltonian

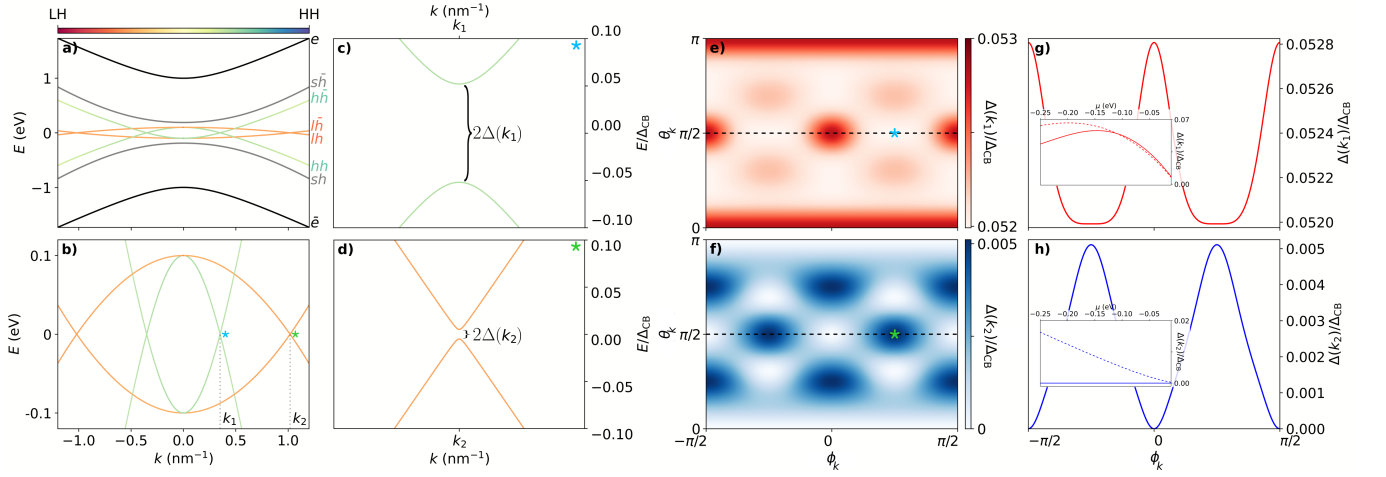


Figure 1. **8KP model.** (a-b) Energy dispersion of the BdG 8KP model along the k ($k_x = k_y$) in-plane direction (perpendicular to the growth direction). Bands are labeled as $\{e/\bar{e}, hh/h\bar{h}, lh/l\bar{h}, sh/s\bar{h}\}$ respectively for electrons, heavy holes, light holes, split-off holes, and their respective particle and time-reversed counterparts. **CB pairing.** (c-d) Gaps opening along the $k_x = k_y$ direction; at (c) $k_1(\pi/4, \pi/2, \mu)$ and (d) $k_2(\pi/4, \pi/2, \mu)$. The color scale determines the LH/HH nature of the band with the quantity $|\langle \text{HH} | \psi \rangle|^2 - |\langle \text{LH} | \psi \rangle|^2 \in [-1, 1]$. (e-f) Gaps as a function of the spherical coordinates ϕ_k and θ_k , such as $(k_x, k_y, k_z) = k(\sin \theta_k \cos \phi_k, \sin \theta_k \sin \phi_k, \cos \theta_k)$; at (e) $k_1(\phi_k, \theta_k, \mu)$ and (f) $k_2(\phi_k, \theta_k, \mu)$. (g-h) Gaps along the black dashed line in (e-f) at (g) $k_1(\phi_k, \pi/2, \mu)$ and (h) $k_2(\phi_k, \pi/2, \mu)$, respectively. (g-h Inset) Gaps as a function of μ ; at (g) k_1 and (h) k_2 , respectively; for $\phi_k = 0$, $\theta_k = \pi/2$ (solid lines) and $\phi_k = \pi/4$, $\theta_k = \pi/2$ (dashed lines). Parameters used: $\Delta_{\text{CB}} = 200 \mu\text{eV}$; $\mu = -0.1 \text{ eV}$; Table I.

is

$$H_{8\text{KP}}^{\text{BdG}} = \begin{pmatrix} H_{cb} - \mu & H_{cb-v} & H_{cb}^{\Delta} & 0_{2 \times 6} \\ H_{cb-v} & H_v - \mu & 0_{6 \times 2} & H_v^{\Delta} \\ H_{cb}^{\Delta \dagger} & 0_{2 \times 6} & \mu - H_{cb}^* & -H_{cb-v}^* \\ 0_{6 \times 2} & H_v^{\Delta \dagger} & -H_{cb-v}^T & \mu - H_v^* \end{pmatrix}. \quad (2)$$

Eq. (2) is the full model which includes the first conduction band (CB, with symmetry Γ_{6c}), described by H_{cb} ; the valence band H_v , which includes light and heavy holes (LH and HH, Γ_{8v}), which are states with total angular momentum $J = 3/2$ described by a $H_{4\text{KP}}$ Kohn-Luttinger Hamiltonian, as well as the split-off (SH, Γ_{7v}) bands with total angular momentum $J = 1/2$. The conduction and valence bands are coupled by the terms H_{cb-v} (see Appendix A for the full expressions).

Fig. 1(a,b) shows the band dispersion along $k_x = k_y$. Along the in-plane direction, the most (less) dispersive valence band is HH-type (LH-type). This behavior is reversed along the z axis, parallel to growth direction, where the LH band is more dispersive than the HH one [59]. We assume that the superconducting proximity effect can induce pairing terms on the conduction and valence bands, H_{cb}^{Δ} and H_v^{Δ} respectively, parametrized by three real parameters $\Delta_{\text{CB}} \neq \Delta_{\text{LH}} \neq \Delta_{\text{HH}}$, not all necessarily non-zero.

Our first step towards an effective 2DHG theory of proximitized Ge holes is to derive and understand the effect of the conduction band within the hole subspace. We first focus on the superconducting pairing contribution that comes from the Γ_{6c} conduction band, i.e.,

$H_{cb}^{\Delta} = i\sigma_y \Delta_{\text{CB}}$ and $H_v^{\Delta} = 0$. As noted in Ref. [54], due to the coupling between CB electrons and holes, mediated by H_{hl-v} in Eq. (2), Δ_{CB} induces an effective pairing in the valence band. Importantly, the induced pairing is momentum-dependent, anisotropic and leads to different gaps in the most and least dispersive bands, $\Delta(k_1)$ and $\Delta(k_2)$, respectively, see Fig. 1(c, d). Here, k_1 (k_2) are defined as the momentum position of the gap in the most (less) dispersive band and depend on the direction as $k_{1,2}(\phi_k, \theta_k) = k_{1,2}(\sin \theta_k \cos \phi_k, \sin \theta_k \sin \phi_k, \cos \theta_k)$. The size of the gaps changes along different directions: in particular, $\Delta(k_1)$ is maximal along $(k_x, 0, 0)$, $(0, k_y, 0)$ and $(0, 0, k_z)$, while the least dispersive band remains gapless along these directions, $\Delta(k_2) = 0$. This anisotropy is best illustrated by plotting the gaps for less symmetric momentum directions, Fig. 1(e-h). The largest gap $\Delta(k_1)$ has a slight angular dependence, while $\Delta(k_2)$ has a stronger dependence, between 0 and $\sim 10\%$ of $\Delta(k_1)$. In addition, the size and positions of these induced gaps depend on μ , see the insets of Fig. 1(g,h), but their values are at best $\Delta_{\text{eff}} \sim 5 - 10\%$ of the parent gap Δ_{CB} .

III. EFFECTIVE 4KP MODEL

In order to get the effect of Δ_{CB} within the hole sector, we use a Schrieffer-Wolff transformation [24] to integrate out the CB contributions and get a 6KP theory involving heavy holes, light holes, and the split-off band. We will further neglect the split-off band, far away in energy (290

meV for Ge), to focus on the HH-LH subspace, which is the most relevant for strained Ge [60] [61]. The resulting Hamiltonian is

$$H_{4\text{KP}}^{\text{BdG}} = \begin{pmatrix} H_{4\text{KP}} - \mu & H_v^\Delta + H_c^\Delta \\ (H_v^\Delta + H_c^\Delta)^\dagger & \mu - H_{4\text{KP}}^* \end{pmatrix}, \quad (3)$$

where $H_{4\text{KP}}$ is the effective Kohn-Luttinger hamiltonian with renormalized parameters, see Appendix B. The pairing term may include a direct contribution to LH and HH valence bands of the form

$$H_v^\Delta = \begin{pmatrix} 0 & 0 & 0 & \Delta_{\text{HH}} \\ 0 & 0 & \Delta_{\text{LH}} & 0 \\ 0 & -\Delta_{\text{LH}} & 0 & 0 \\ -\Delta_{\text{HH}} & 0 & 0 & 0 \end{pmatrix}, \quad (4)$$

and an effective contribution mediated by their coupling to the CB,

$$H_c^\Delta = \frac{\Delta_{\text{CB}}}{E_g - 2\mu} \times \begin{pmatrix} 0 & -R_\Delta & -S_\Delta & -P_\Delta - Q_\Delta \\ R_\Delta & 0 & P_\Delta - Q_\Delta & S_\Delta^\dagger \\ S_\Delta & -P_\Delta + Q_\Delta & 0 & -R_\Delta^\dagger \\ P_\Delta + Q_\Delta & -S_\Delta^\dagger & R_\Delta^\dagger & 0 \end{pmatrix}, \quad (5)$$

$$P_\Delta = -\frac{\hbar^2}{2m_0} \gamma_\Delta (k_x^2 + k_y^2 + k_z^2),$$

$$Q_\Delta = -\frac{\hbar^2}{4m_0} \gamma_\Delta (k_x^2 + k_y^2 - 2k_z^2), \quad x\check{z}$$

$$R_\Delta = \frac{\hbar^2}{4m_0} \sqrt{3} \gamma_\Delta [(k_x^2 - k_y^2) - 2ik_x k_y],$$

$$S_\Delta = -\frac{\hbar^2}{2m_0} \sqrt{3} \gamma_\Delta k_- k_z,$$

where E_g is the band gap, m_0 the bare electron mass, and $\gamma_\Delta = 7.38$ is calculated from the band parameters of Ge, see Appendix B.

The symmetry of the induced effective pairing in the hole band is inherited from the lowest Γ_{6c} conduction band which has spherical symmetry, leading to a single effective Luttinger parameter γ_Δ [54]. On the other hand, the 4KP Hamiltonian has a lower symmetry and is characterized by three Luttinger parameters γ_1 , γ_2 , and γ_3 . This mismatch in symmetries induces non-trivial anisotropies of the effective pairings in the eigenbasis of the 4KP Hamiltonian as shown in Fig. 1(e,f). The expressions for the in-plane components ($\theta_k = \pi/2$), in the eigenbasis of $H_{4\text{KP}}$, are

$$\Delta(\mathbf{k}_1) \approx \frac{\Delta_{\text{CB}} \gamma_\Delta \hbar^2 |\mathbf{k}_1|^2}{(E_g - 2\mu) m_0} \left[1 - \frac{3\gamma_-^2 \sin^2 2\phi_k}{32\gamma_+^2} (5 + 3 \cos 4\phi_k) \right]$$

$$\Delta(\mathbf{k}_2) \approx \frac{\Delta_{\text{CB}} \gamma_\Delta \hbar^2 |\mathbf{k}_2|^2}{(E_g - 2\mu) m_0} \left[\frac{3\gamma_-^2 \sin^2 2\phi_k}{32\gamma_+^2} (5 + 3 \cos 4\phi_k) \right], \quad (6)$$

where we have expanded in γ_-/γ_+ up to second order, with $\gamma_\pm = \gamma_3 \pm \gamma_2$ the Luttinger parameters of the hole bands. The anisotropic behavior is proportional to γ_- , which quantifies the lack of spherical symmetry of the system. Eq. (6) displays the complementary behavior of $\Delta(k_1)$ and $\Delta(k_2)$ shown in Fig. 1. Besides, Eq. (5) displays pairing terms that couple the different bands. Hence, at points where there is a crossing between holes and their time-reversed states with a different spin, an anticrossing may occur. For a detailed benchmarking between the effective 4KP and the original 8KP model, see Appendix C.

IV. EFFECTIVE 2DHG 4KP MODEL

Now we apply this effective theory to the experimentally relevant scenario of a 2DHG in Ge. We focus on strained Ge/Ge_{1-x}Si_x quantum wells with a depth of L_W . The HH and LH bands are split by E_{hl} due to their different effective masses in the confinement direction. The different lattice constants of the GeSi barriers and the Ge well introduce an extra energy splitting E_{hl}^{strain} [62]. Within the hard-wall approximation for confinement, we use the Bastard wavefunctions [63] to estimate E_{hl} and the spin splitting, see Appendix D.

Assuming $L_W = 16$ nm and a Si content of 20%, $E_{hl} \approx 70$ meV for reasonable vertical electric fields $|F| < 5$ MV/m. The vertical electric field breaks the inversion symmetry, and the effective mass difference between HH and LH induces a Rashba SOI within the hole subspace. In particular, for the vertical ground state, we get $\langle 0_H(z) | p_z | 0_L(z) \rangle = i\alpha_0$, where α_0 is proportional to F (see Appendix D). The finite value of α_0 induces an effective cubic in momentum SOI within the HH subspace [24] and leads to a spin-splitting in k-space for both HH and LH.

We first identify the different regimes in terms of the chemical potential. In Fig. 2 we show the bands and Fermi-level crossing points k_i as a function of μ for $F = 0$. Fig. 2(a) shows that, for large negative values of μ , both HH and LH bands cross the Fermi level and there are up to four different crossings. In this regime, the bands exhibit strong HH-LH hybridization, as can be seen from the color code. In Fig. 2(b) we show an intermediate regime where the value of μ leads to only two Fermi-level crossings, yet they exhibit a strong HH-LH hybridization. Finally, only when $|\mu| \ll E_{hl}$ the two bands crossing have approximately well-marked HH behavior, see Fig. 2(c). Due to their different effective masses, HH and LH bands anticross in k space at the value $\hbar k_{h,l} = \sqrt{E_{hl} m_0 / \gamma_2}$ (marked as a green star in Fig. 2); this value of k can be understood as an approximate regime boundary as shown in Fig. 2(d): as HH-LH bands become strongly hybridized, perturbation theory fails and a full 4-level model must be used. Conversely, perturbation theory

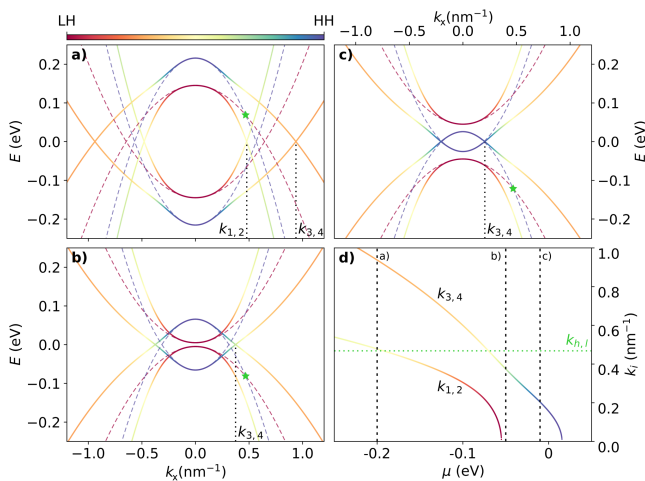


Figure 2. **2DHG 4KP regimes for different μ .** (a) Bands along the k_x direction for $\mu = -0.2$ eV. At $\mathbf{k} = 0$, the two spin-degenerate hole bands, split in energy by E_{hl} , cross the Fermi level at momenta $k_{1,2}$ and $k_{3,4}$, respectively. While these two bands retain their well-defined HH and LH character at low momenta, they gradually mix and hybridize as momentum grows. (b) Bands along the k_x direction for $\mu = -0.05$ eV, where only one spin-degenerate band crosses the Fermi level, yet this band exhibits strong HH-LH hybridization. (c) Bands along the k_x direction for $\mu = -0.01$ eV, where the crossing band has a well defined HH character. (d) Position of the different gaps in quasi-momentum k_i for $F = 0$ along the k_x direction. Black dashed vertical lines indicate the different values of μ used in panels (a-c). The green dotted line in panel (d) and the green star marker in panels (a-c) indicate when the HH and the LH band dispersions cross in momentum $\hbar k_{h,l} = \sqrt{E_{hl}m_0/\gamma_2}$, calculated under the assumption of decoupled bands –dashed curves in panels (a-c). Parameters used: $\Delta_{CB} = 200$ μeV ; $F = 0$; Table I; Appendix D.

only makes sense if, for a given μ , the bands cross the Fermi level well before this hybridization point $k_{h,l}$. In Fig. 2(d), case a) would represent a situation well outside the validity range of perturbation theory, while case c) would correspond to a situation in which perturbation theory could be applied, since the bands crossing the Fermi level have a well defined HH character. However, and since, in general, the precise value of μ is largely unknown, we would like to emphasize that even in situations where only HH bands are expected to participate in the proximitized 2DHG, a full 4-level model, like the one used here, seems to be the correct approach.

A. Analytical pairing expressions

Given that perturbation theory is only valid in a small window of μ , we analyze our problem with the full 4-bands Hamiltonian and the vertical Bastard wavefunctions. Besides, an exact treatment circumvents the issue

with diverging Fermi surfaces in effective HH theories with superconductivity [53]. Within this approximation, the 4-band Kohn-Luttinger Hamiltonian H_{4KP} in Eq. (3) can be diagonalized analytically at zero magnetic field. The procedure of this exact diagonalization is explained in Appendix E and yields

$$H_{4KP}^{(d)} = UH_{4KP}U^\dagger = \text{diag}(E_2, E_1, E_4, E_3), \quad (7)$$

where U is the unitary diagonalizing the hole Hamiltonian. Conversely, the time-reversed Hamiltonian is diagonalized by $U' = U^*(-\mathbf{k})$. The energies E_i are associated with the states that cross the Fermi level at k_i in Figs. 2 and 3. Hence, at $\mathbf{k} = 0$, $E_{1,2}$ are eigenvalues of the LH states and $E_{3,4}$ are eigenvalues of the HH band. Note that these energies are not written in an explicit manner including their full dependence on parameters $E_i(k_x, k_y, F, \mu)$ for simplicity. The eigenbasis can be expressed in terms of a rotated Nambu basis as $\tilde{\Psi} = (\tilde{b}_{2,\uparrow}, \tilde{b}_{1,\downarrow}, \tilde{b}_{4,\uparrow}, \tilde{b}_{3,\downarrow}, \tilde{b}_{2,\uparrow}^\dagger, \tilde{b}_{1,\downarrow}^\dagger, \tilde{b}_{4,\uparrow}^\dagger, \tilde{b}_{3,\downarrow}^\dagger)^T$, where $\tilde{b}_{i,\tilde{s}}$ destroys a hole band with eigenenergy E_i and spin \tilde{s} aligned or anti-aligned with the spin-orbit interaction. Importantly, on this basis, the pairing block of the Hamiltonian takes the form

$$H^\Delta{}^{(d)} = UH^\Delta U'^\dagger = \Delta_{ij} = \begin{pmatrix} \tilde{\Delta}_l(\mathbf{k}_1, \mathbf{k}_2) \cdot \boldsymbol{\sigma} & \tilde{\Delta}_{lh}(\mathbf{k}_i) \cdot \boldsymbol{\sigma} \\ \tilde{\Delta}_{hl}(\mathbf{k}_i) \cdot \boldsymbol{\sigma} & \tilde{\Delta}_h(\mathbf{k}_3, \mathbf{k}_4) \cdot \boldsymbol{\sigma} \end{pmatrix}, \quad (8)$$

where H^Δ may include pairing amplitudes between any of the bands, and we introduce the block operators $\tilde{\Delta}_i$ as the pairing components Δ_{ij} grouped in blocks and projected to the space of Pauli matrices in the Rashba basis, such that

$$\tilde{\Delta}_i \cdot \boldsymbol{\sigma} = \sum_{j=\{0,x,y,z\}} \tilde{\Delta}_{i,j} \sigma_j. \quad (9)$$

The diagonal blocks $\tilde{\Delta}_{l/h}$ are intraband pairing terms associated to the bands with LH/HH character at low k values, and the off-diagonal blocks $\tilde{\Delta}_{lh/hl}$ are interband pairing terms related to different anticrossings between hole and their time-reversed partners of different bands away from the Fermi level. Each of these blocks contain triplet and singlet components. In this basis, the triplets correspond to the 0 and z components, while the singlets correspond to the x and y components of the intraband terms. Eq. (8) is one of the main results of our paper and allows us to obtain explicit pairing terms for the different hole bands. In what follows, we provide analytical expressions of these pairings terms expanded up to third order in momenta, and refer to Appendix E for the exact expressions.

Focusing on the intraband blocks, and assuming that the proximity effect originates from the conduction band only, the expansions of the non-zero contributions com-

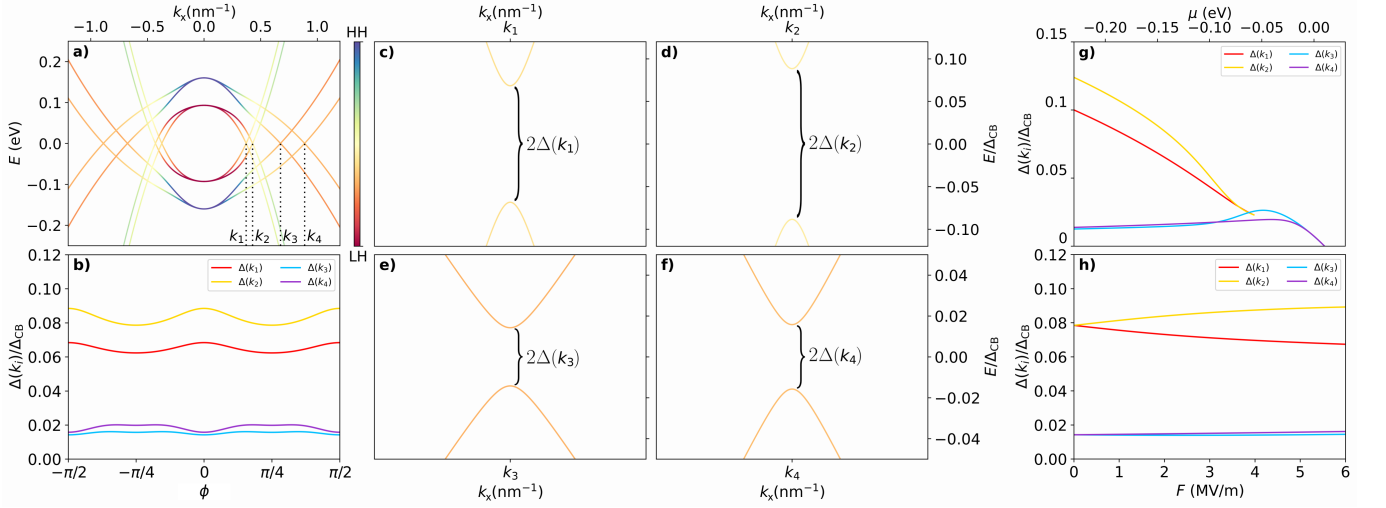


Figure 3. **Induced pairings in the 2DHG 4KP model with SC proximity coming from the CB only.** (a) Energy dispersion of the BdG 2DHG 4KP model along the k_x direction. **CB pairing.** (b) SC pairing as a function of the polar coordinate ϕ_k , such as $(k_x, k_y) = k(\cos \phi_k, \sin \phi_k)$; at $k_{1,2,3,4}(\phi_k, \mu)$. (c-f) Gaps opening along the k_x direction; at $k_{1,2,3,4}(0, \mu)$, respectively. (g-h) Gaps opening at $\phi_k = 0$ as a function of (g) μ with $F = 5$ MV/m, and (h) F with $\mu = -0.15$ eV. Parameters used: $\Delta_{CB} = 200$ μeV ; $\mu = -0.15$ eV and $F = 5$ MV/m unless otherwise stated; Table I; Appendix D.

ing from $H^\Delta = H_{(cb)}^\Delta$, are:

$$\begin{aligned} \frac{\tilde{\Delta}_{l,0}^{(c)}}{\Delta_{CB}} &= \frac{\tilde{\Delta}_{h,0}^{(c)}}{\Delta_{CB}} \approx \frac{-3i\alpha_R\gamma_\Delta}{2(E_g - 2\mu)m_0} p^2 e^{3i\phi_k}, \\ \frac{\tilde{\Delta}_{l,x}^{(c)}}{\Delta_{CB}} &= \frac{\tilde{\Delta}_{h,x}^{(c)}}{\Delta_{CB}} \approx \frac{3i\alpha_R\gamma_\Delta (\gamma_+ - i\gamma_- e^{4i\phi_k})}{2(E_g - 2\mu)m_0\gamma_3} p^2 e^{3i\phi_k}, \\ \frac{\tilde{\Delta}_{l,z}^{(c)}}{\Delta_{CB}} &\approx \frac{-i\gamma_\Delta}{4(E_g - 2\mu)} (p^2 + 4(p_z^2)) e^{3i\phi_k}, \\ \frac{\tilde{\Delta}_{h,z}^{(c)}}{\Delta_{CB}} &\approx \frac{3i\gamma_\Delta}{4(E_g - 2\mu)} p^2 e^{3i\phi_k}, \end{aligned} \quad (10)$$

where α_R is a linear-in-momentum adimensional Rashba coefficient $\alpha_R = \gamma_3\alpha_0 p / (E_{hl}m_0)$, $p = \hbar\sqrt{k_x^2 + k_y^2}$, and $\phi_k = \arctan(k_x/k_y)$. These expressions feature both singlet and triplet types of pairing terms.

If, on the other hand, we assume that direct proximity effect is possible in the valence band with pairing terms $H^\Delta = H_v^\Delta$ including both Δ_{HH} and Δ_{LH} , see Eq. (4), the non-zero intraband components are

$$\begin{aligned} \frac{\tilde{\Delta}_{l,0}^{(v)}}{\Delta_H} &= \frac{\tilde{\Delta}_{h,0}^{(v)}}{\Delta_H} \approx -i\alpha_R\zeta e^{3i\phi_k}, \\ \frac{\tilde{\Delta}_{l,z}^{(v)}}{\Delta_{LH}} &\approx i \left(1 - \frac{6\bar{\Delta}_H}{\Delta_{LH}} \alpha_R^2 \right) e^{3i\phi_k}, \\ \frac{\tilde{\Delta}_{h,z}^{(v)}}{\Delta_{HH}} &\approx i \left(1 - \frac{6\bar{\Delta}_H}{\Delta_{HH}} \alpha_R^2 \right) e^{3i\phi_k}, \end{aligned} \quad (11)$$

where we have defined an average pairing $\bar{\Delta}_H = (\Delta_{HH} + \Delta_{LH})/2$ and the adimensional quantity $\zeta = 6(\gamma_+ -$

$\gamma_- e^{4i\phi_k}) p^2 / (E_{hl}m_0)$. Note that, in contrast to Eq. (10), the effective pairings in Eq. (11) only feature triplet components since the x and y components are identically zero, see Appendix E.

B. Conduction band contributions to the gap

We now analyze some representative results corresponding to the case $\Delta_{HH} = \Delta_{LH} = 0$ and $\Delta_{CB} \neq 0$. We turn on the electric field in Fig. 3(a), where we show the band structure along the k_x direction after projecting the vertical motion to the ground state. All four crossing points between bands may display a gap, as seen in Fig. 3(b-f). The value of the gap at these different crossing points is heavily dependent on the nature of the bands and, strikingly, exhibits a certain degree of gate-tunability through the vertical electric field F and the chemical potential μ . As can be seen in Fig. 3, this gap can go up to 10% of Δ_{CB} for the first band crossings in the large negative μ regime. Hence, assuming that the parent superconducting gap comes entirely from Al, with $\Delta_{Al} \approx 200\mu\text{eV}$, the induced superconducting gap through the conduction band can reach values of around $20\mu\text{eV}$ in the valence band. For $k_{3,4}$, the value of the gap is about five times smaller: for Al, it would be a few μeV at most.

To further understand the nature of the induced superconductivity, we go to the expressions of the pairings in the eigenbasis in Eq. (10). These expressions already provide an intuitive framework to analyze the pairing potentials in Fig. 3. In particular, the terms that go with

either the identity or σ_z are directly related to the gaps we observe. The presence of σ_0 and σ_z pairing terms as well as their intrinsic dependence on k lead to each gap displaying differences in their dependence with μ and F . The gaps are mainly dominated by $\tilde{\Delta}_{l,z}(\mathbf{k}_1, \mathbf{k}_2)$ and $\tilde{\Delta}_{h,z}(\mathbf{k}_3, \mathbf{k}_4)$, which are $\propto p^2$, a kinetic term. For $\tilde{\Delta}_{l,z}$ there is an extra p_z^2 dependence, which is responsible for the relative shift of $\Delta(k_1)$, $\Delta(k_2)$ compared to $\Delta(k_3)$, $\Delta(k_4)$ in Fig. 3(b). In Fig. 3(g), we show a non-trivial dependence with μ . As μ goes from more negative values to zero, the gaps tend to decrease. This is a consequence of their proportionality with k : lower values of $|\mu|$ decrease the values of k_i , leading to lower kinetic pairing terms.

The gap dependence on vertical electric field in Fig. 3(h) can be identified from the identity components $\tilde{\Delta}_{l/h,0}$ in Eq. (10), which are directly related to the cubic Rashba interaction, that introduce a gate-dependence through the Rashba coefficient $\alpha_0(F_z)$. The direct dependence on p_z^2 induces a stronger field dependence in $\Delta(k_{1,2})$ than that of $\Delta(k_{3,4})$, as can be seen in Fig. 3(h). Finally, the singlet contributions $\tilde{\Delta}_{i=1/h,x}$ also arise from the cubic Rashba interaction. Interestingly, this singlet pairing term appears even in the absence of a magnetic field and is proportional to the vertical electric field. Physically, the singlet pairing term does not influence the gap at zero magnetic field but induces anticrossings between hole and their time-reversed partners with opposite spin outside the Fermi level.

C. Direct heavy-hole and light-hole contributions to the gap

The measured gaps in experiments can be close to the parent superconducting gap [44, 45, 47, 50] unlike our much smaller prediction (at most $\sim 10\% \Delta_{\text{CB}}$) when assuming a CB-only proximity effect, see Sec. IV B. Even though symmetry arguments [54] may imply that the only direct proximity effect can be induced by the CB, the superconductor-semiconductor interface reduces the symmetry and may introduce direct tunneling between the superconductor electrons and the semiconductor valence band [64]. It is then relevant to introduce Δ_{HH} and Δ_{LH} .

In Fig. 4 we show the dependence of the induced pairings on the chemical potential μ . At low values of $|\mu|$, in the perturbative regime, the bands crossing the Fermi level at k_3 and k_4 have strong HH character. Consequently, there is a strong contribution to the gaps in these bands coming directly from the pairing term Δ_{HH} , such that $\Delta(k_{3,4}) \approx \Delta_{\text{HH}}$, see Fig. 4(a). As μ gets more negative, LH and HH bands hybridize, reducing the relative weight of Δ_{HH} , hence $\Delta(k_{3,4})$ decrease. $\Delta(k_{1,2})$, with a well-marked LH character at low values of k , exhibit the opposite behavior, starting from $\mu \approx -E_{hl}$.

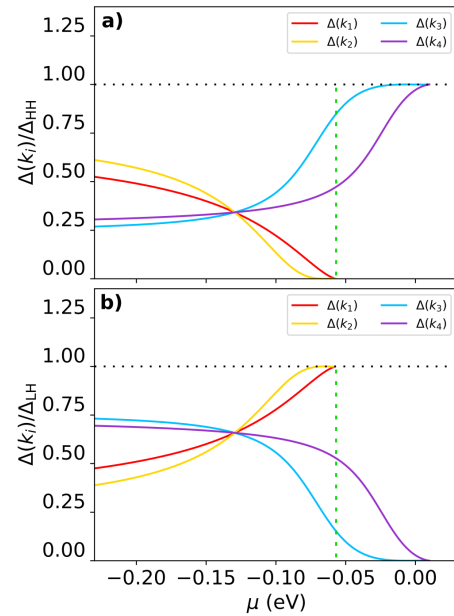


Figure 4. **Direct LH/HH pairing.** Gaps $\Delta(k_{1,2,3,4})$ along the k_x direction, as a function of μ for (a) HH and (b) LH direct pairing. The vertical dashed line indicates $\mu = -E_{hl}$, where $\Delta(k_1, k_2)$ emerge. Parameters used: $\Delta_{\text{LH/HH}} = 200 \mu\text{eV}$; $F = 5 \text{ MV/m}$; Table I; Appendix D.

These trends are exchanged when Δ_{LH} is switched on, Fig. 4(b).

This picture is consistent with Eq. (11), where we find triplet contributions with a series of corrections that can be interpreted as the effect of mixing HH and LH states. Proportional to the identity, we find another correction that is linear with the electric field and comes from the cubic Rashba interaction. The competing σ_0 and σ_z terms introduce a spin-dependent gap size for states within the same band that is tunable mostly through the value of μ , which changes the values of k_i at which the Fermi level crossings occur.

D. Disorder effects: mixed heavy-light contributions

Interface mismatches and the existence of intermediate barriers, for example amorphous oxides, may introduce new terms in the Hamiltonian due to the reduced symmetry. This occurs even in quite compatible interfaces, such as Si/SiGe and GaAs/AlGaAs [27, 65]. We therefore generalize our expressions to include constant pairing terms mixing HHs and LHs with reduced symmetry. These terms are analogous to strain-induced terms, where deformations breaking the symmetry along differ-

ent directions lead to the Bir-Pikus Hamiltonian [62]:

$$H_m^\Delta = \begin{pmatrix} 0 & \Delta_R e^{i\chi_R} & \Delta_S e^{i\chi_S} & 0 \\ -\Delta_R e^{i\chi_R} & 0 & 0 & -\Delta_S e^{-i\chi_S} \\ -\Delta_S e^{i\chi_S} & 0 & 0 & \Delta_R e^{-i\chi_R} \\ 0 & \Delta_S e^{-i\chi_S} & -\Delta_R e^{-i\chi_R} & 0 \end{pmatrix}. \quad (12)$$

Δ_R and Δ_S can be written as $\Delta_R e^{i\chi_R} = (\Delta_{YY} - \Delta_{XX}) + i\Delta_{XY}$ and $\Delta_S e^{i\chi_S} = \Delta_{XZ} + i\Delta_{YZ}$, illustrating broken symmetries along different directions in analogy to strain in the Bir-Pikus Hamiltonian. In Ref. [66] similar terms arise from tunneling between the superconductor and semiconductor along different directions. We follow the same procedure as in subsection IV A and write this pairing matrix in the frame that diagonalizes the 4-bands Kohn-Luttinger Hamiltonian. For the mixed intraband corrections $\tilde{\Delta}_{l/h}^{(m)}$ we get:

$$\begin{aligned} \frac{\tilde{\Delta}_{l,0}^{(m)}}{\Delta_R} &= \frac{\tilde{\Delta}_{h,0}^{(m)}}{\Delta_R} \approx 2i\sqrt{3}\alpha_R e^{3i\phi_k} \cos(2\phi_k + \chi_R) \\ \frac{\tilde{\Delta}_{l,x}^{(m)}}{\Delta_R} &= -\frac{\tilde{\Delta}_{h,x}^{(m)}}{\Delta_R} \approx 2\sqrt{3}\alpha_R e^{3i\phi_k} \sin(2\phi_k + \chi_R) \\ \frac{\tilde{\Delta}_{l,y}^{(m)}}{\Delta_S} &= \frac{\tilde{\Delta}_{h,y}^{(m)}}{\Delta_S} \approx 2\sqrt{3}\alpha_R e^{3i\phi_k} \sin(\phi_k + \chi_S) \\ \frac{\tilde{\Delta}_{l,z}^{(m)}}{\Delta_R} &= \frac{\tilde{\Delta}_{h,z}^{(m)}}{\Delta_R} \approx \frac{-i\zeta e^{3i\phi_k}}{2\sqrt{3}} \cos(2\phi_k + \chi_R). \end{aligned} \quad (13)$$

Interestingly, mixed terms Δ_S introduce singlet terms, while those coming from Δ_R introduce both singlet and triplet pairing in the eigenbasis of the 4-bands Hamiltonian. All terms exhibit a p-type dependence in momentum, coming from the Rashba interaction, except the z -term which has a kinetic nature with cubic symmetry. Moreover, their low-symmetry nature leads to highly directional contributions, introducing rotations to the in-plane momentum angle.

In Fig. 5(a), we illustrate the effect of these pairing terms as a function of μ . As μ decreases, the pairing terms coming from Δ_R increase their influence for all different gaps. However, this increase is not always monotonous, and there can be sign changes when the 0-component exactly cancels out the z -component for a specific spin state leading to the gap closures in Fig. 5(a). Furthermore, the phase χ_R breaks the cubic symmetry and rotates the preferred directions in the different gaps, see Fig. 5(b). Taking $\chi_R = \pi/4$ (dashed line) induces a directional correction that reduces the symmetry of the gaps.

V. EXPERIMENTAL SIGNATURES

We address now the question of how to distinguish among all the possible pairing mechanisms discussed

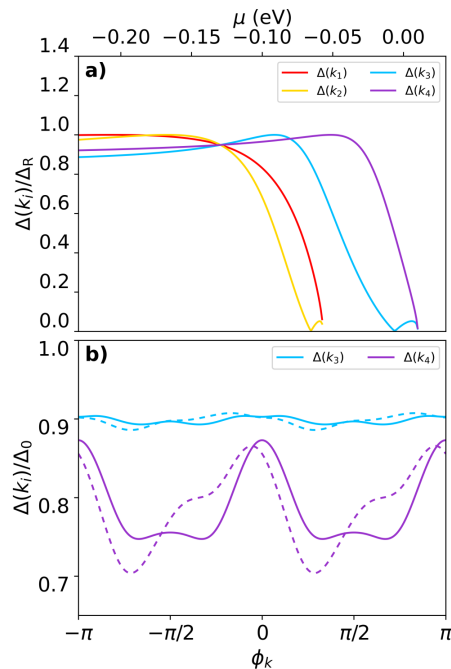


Figure 5. **Mixed LH-HH pairing.** (a) Gaps $\Delta(k_1, k_2, k_3, k_4)$ and their dependence on μ for mixed pairing $\Delta_R = 200 \mu\text{eV}$ and $\chi_R = 0$. (b) Gaps $\Delta(k_3, k_4)$ as a function of ϕ_k for $\mu = -0.01$ eV for $\Delta_{\text{HH}} = 180 \mu\text{eV}$ and $\Delta_R = 20 \mu\text{eV}$ with $\chi_R = 0$ (solid) and $\chi_R = \pi/4$ (dashed).

above. Specifically, we focus on the intricate response of the proximitized 2DHG to external magnetic fields and discuss how they modify the band profiles and the induced gaps, giving rise to unique experimental signatures. They include distinct DOS (a quantity that can be directly linked to tunneling spectroscopy experiments) for both out-of-plane and in-plane magnetic fields as well as the emergence of strongly anisotropic Bogoliubov-Fermi surfaces.

A. Magnetic field effects

In proximitized Rashba semiconductors, the Zeeman term competes with the SOI leading to magnetic-field tunable spin triplet and spin singlet pairing terms and, hence, magnetic-dependent gaps [67–70]. Given the strong anisotropic response of holes to magnetic fields, we expect to find strong anisotropic behavior in the superconducting gaps as well. We focus now on the effect of Zeeman terms. Magneto-orbital corrections due to the vector potential will be discussed in Appendix G.

In the large negative μ regime, strong Rashba spin splitting appears near the crossings at the Fermi level k_i , which is expected since the Rashba spin-splitting is, effectively, cubic in momentum for Ge holes. In this regime, the spin is strongly polarized and the magnetic

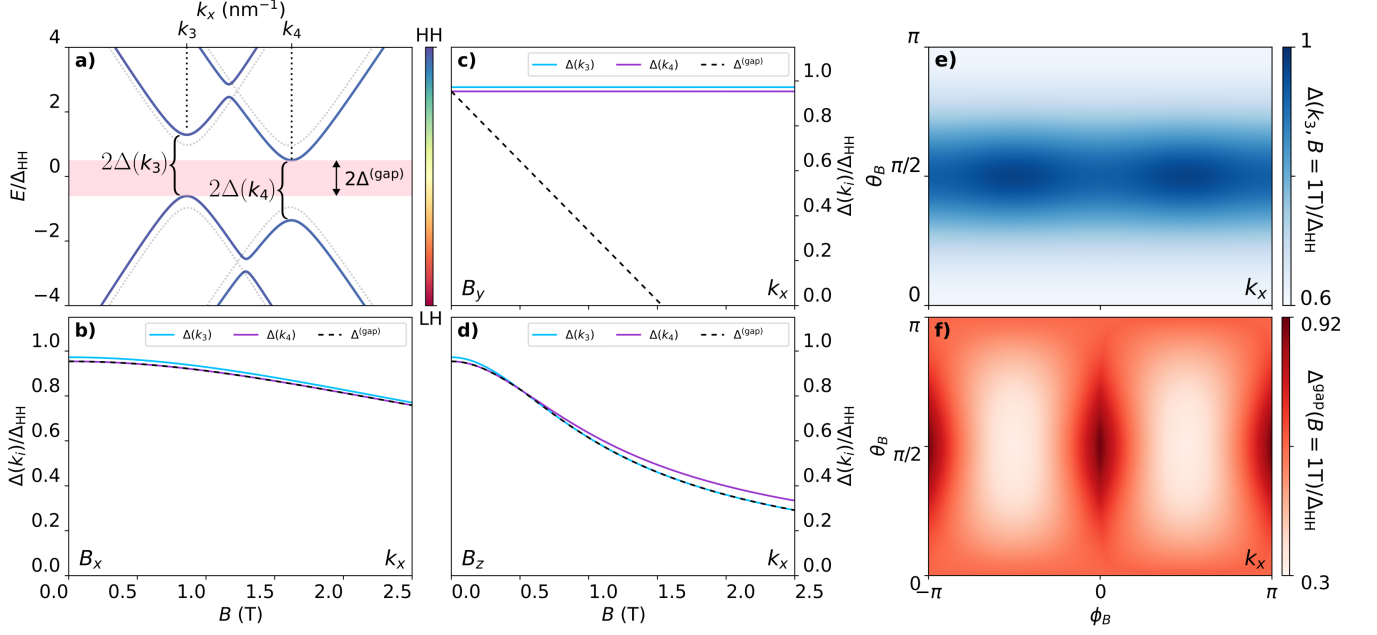


Figure 6. **Magnetic-field dependence of pairings with direct HH contribution.** (a) Tilted bands as a function of k_x around the Fermi level crossings at k_i for $\mathbf{B} = 1/\sqrt{2}(1, 1, 0)$ (solid blue) and $\|\mathbf{B}\| = 0$ (dashed grey). The gap $\Delta^{(\text{gap})}$ is shown as a pink band around $E = 0$ and the pairing terms $\Delta(k_i)$ are associated to the Fermi-level anticrossings. (b-d) Dependence of pairings $\Delta(k_3)$ and $\Delta(k_4)$ on the strength of a magnetic field for: (b) B_x , (c) B_y , and (d) B_z . The value of the spectral gap $\Delta^{(\text{gap})}$ is given as a dashed line. (e) Dependence of pairing $\Delta(k_3)$ on the orientation of a magnetic field with $\mathbf{B} = (\sin \theta_B \cos \phi_B, \sin \theta_B \sin \phi_B, \cos \theta_B)$ T, along the k_x direction. (f) Dependence of spectral gap $\Delta^{(\text{gap})}$ on the orientation of a magnetic field with $|\mathbf{B}| = 1$ T, along the k_x direction. Parameters used: $\Delta_{\text{HH}} = 200 \mu\text{eV}$; $\mu = -0.01$ eV; $F = 0.5$ MV/m; Table I; Appendix D.

field required to modify this polarization and influence the nature of the gap is too large to be experimentally feasible. Consequently, magnetic signatures on the gap are expected to be more evident at small values of $|\mu|$, where k_i are not too large and the Zeeman field can compete with the cubic-in-momentum spin splitting. In the low $|\mu|$ regime, the excitations crossing the Fermi level at $k_{3,4}$ have strong HH character, therefore, we focus on the case $\Delta_{\text{HH}} \neq 0$. In this regime, we expand the spin splitting $\delta_h = E_4 - E_3$ to lowest order in momentum in the eigenbasis, using Eq. (7), to obtain:

$$\delta_h = E_4 - E_3 \approx |\zeta \alpha_R| E_{hl}. \quad (14)$$

Depending on the magnetic field orientation, there can be different types of signatures in the gap, as illustrated in Figs. 6(e,f). In particular, in-plane magnetic fields tilt the spectrum, potentially leading to the closing of the spectral gap [56–58] (even though each band still shows a finite pairing). This distinction between the pairing terms and the spectral gaps is illustrated in Fig 6(a), where a zoom near the Fermi level crossings around k_3 and k_4 shows the tilt in the spectrum (lack of mirror symmetry around $E = 0$). The effective triplet pairings $\Delta(k_i)$ are defined as half the minimal energy distance in k between hole and the time-reversed spectra, while the spectral gap $\Delta^{(\text{gap})}(\phi_k)$ is given by the energy range

where the bands never cross for any k .

We focus first on the effective pairings; in Fig. 6(b-e), we show the dependence of the size of the triplet pairings at k_3 and k_4 against magnetic field in different directions. These pairing amplitudes are tunable mainly using vertical magnetic fields, see Fig. 6(d,e) along k_x . In particular, Fig. 6(e) shows a map of the pairing as a function of magnetic field orientation taking $\|\mathbf{B}\| = 1$ T. In this scenario, the pairing is strongly normalized when $B \parallel \hat{z}$ but in-plane magnetic fields cause only a small anisotropy.

The anisotropic behavior of the pairings in Fig. 6 can be understood in terms of geometrical relationships. In the original basis, the Zeeman Hamiltonian is $H_Z = -2\mu_B \kappa \mathbf{J} \cdot \mathbf{B} - 2q\mu_B \mathbf{J}^3 \cdot \mathbf{B}$, where \mathbf{J} and $\mathbf{J}^3 = (J_x^3, J_y^3, J_z^3)$ are vectors of spin 3/2 matrices, $\kappa = 3.41$, and $q = 0.06$ in Ge. In the eigenbasis, the Zeeman term can be written as:

$$H_{Z,34}^{(d)} = \frac{1}{2} \mu_B \boldsymbol{\sigma} \cdot \begin{pmatrix} 0 & 0 & g_{xz} \\ g_{yx} & g_{yy} & 0 \\ g_{zx} & g_{zy} & 0 \end{pmatrix} \cdot \mathbf{B}, \quad (15)$$

where the g_{zx} and g_{zy} characterize the in-plane Zeeman terms that are parallel to the Rashba field and, hence, compete directly with the Rashba spin-splitting δ_h , while

g_{yx} and g_{yy} (g_{xz}) characterize the in-plane (out-of-plane) Zeeman terms that are perpendicular to the Rashba spin-splitting. These g-factors can be approximated as:

$$\begin{aligned} g_{zx} &\approx 3q \sin 3\phi_k - |\zeta| \kappa \sin \phi_k, \\ g_{yx} &\approx 3q \cos 3\phi_k - |\zeta| \kappa \cos \phi_k, \\ g_{zy} &\approx 3q \cos 3\phi_k + |\zeta| \kappa \cos \phi_k, \\ g_{yy} &\approx -3q \sin 3\phi_k - |\zeta| \kappa \sin \phi_k, \\ g_{xz} &\approx 6\kappa + \frac{27}{2}q. \end{aligned} \quad (16)$$

In Appendix G, we estimate via perturbation theory the strong renormalizations of the g-factors [71] caused by the vector potential, not included here. Note that the in-plane terms g_{ix} and g_{iy} exhibit a strong in-plane anisotropic behavior through their dependence on ϕ_k . Compared to the hole g-matrix, the g-matrix and spin-splitting of the time-reversed states have opposite signs $\bar{g}_{ij} = -g_{ij}$ for $i \neq z$ and $\bar{\delta}_h = -\delta_h$. The only exception are the g-factors associated to Zeeman terms that are parallel to the Rashba interaction, in which case we find $\bar{g}_{zi} = g_{zi}$, introducing a direct competition with the Rashba splitting that tilts the spectrum [57, 58].

When the Zeeman field points along the y direction, we get Zeeman terms that are only parallel to the Rashba SOI for $k_y = 0$ as in Fig. 6(c), leaving the pairing Hamiltonian invariant, yet introducing a tilt in the spectrum. As a result, the triplet pairings remain constant along $\mathbf{B} \parallel \hat{y}$, Figs. 6(c, e). As can be deduced from the g-factor expressions, the magnetic field that leaves the pairing invariant heavily depends on the orientation in k -space. When $\mathbf{B} \parallel \hat{x}$, as in Fig. 6(b), we get Zeeman contributions that are perpendicular to the Rashba field, however, the HH in-plane g-factors are quite small, suppressed by E_{hl} , and, while there is a visible renormalization of the triplet pairing, this is relatively small for $\|\mathbf{B}\| = 1\text{T}$. Overall, the spin-splitting tends to dominate over the in-plane Zeeman terms as long as $\alpha_0 p / m_0 \gg \kappa \mu_B B_{\parallel}$.

For a vertical magnetic field we get a perpendicular contribution to the Rashba field and the g-factor g_{xz} is not suppressed, leading to a change in the spin polarization and a stronger triplet pairing renormalization. Geometrically, when $B_z \neq 0$, the pairing Hamiltonian in the spin space is rotated around the y direction. At $B = 0$, low k and $|\mu|$, the pairing term in Eq. (11) can be approximated to $\tilde{\Delta}_d^{(v)}(\mathbf{k}_3, \mathbf{k}_4) \cdot \boldsymbol{\sigma} \approx i\Delta_{\text{HH}}\sigma_z$ while, when $B_z \neq 0$, it becomes

$$\frac{\tilde{\Delta}_d^{(v)}(\mathbf{k}_3, \mathbf{k}_4) \cdot \boldsymbol{\sigma}}{\Delta_{\text{HH}}} \approx \frac{i(\delta_h \sigma_z - g_{xz} \mu_B B_z \sigma_x)}{\sqrt{\delta_h^2 + (g_{xz} \mu_B B_z)^2}}. \quad (17)$$

Interestingly, Eq. (17) resembles the familiar result of a proximitized Rashba semiconductor [1–4] with the main difference of the cubic-in-momentum dependence of δ_h suggesting an effective f-type superconducting pairing. Furthermore, we see clearly that, as B_z grows, the original triplet pairing becomes more a singlet-type contribu-

tion. For the rotation of the pairing terms under a general magnetic field, we refer to Appendix F. The emergence of a singlet contribution introduces another anti-crossing in the spectrum between k_3 and k_4 at non-zero magnetic fields in Fig. 6(a).

The spectral gap exhibits a clearly distinct behavior to the pairing amplitude, as shown in Fig. 6(f). In the case where Zeeman contributions are purely transverse to the Rashba interaction, the spectral gap $\Delta^{(\text{gap})}$ is equivalent to the minimal value of the two pairings $\Delta(k_3)$ and $\Delta(k_4)$. This is exactly what happens along k_x for finite fields along B_x and B_z , Fig. 6(b,d). In contrast, any Zeeman component parallel to the Rashba field, introduces a tilt in the spectrum. Along k_x , any B -field component parallel to \hat{y} introduces this tilt and, hence, a reduction in the gap occurs without a concomitant reduction of the pairing, see Fig. 6(c). As a result, in Fig. 6(f), we see a strong suppression of the gap as long as there is any B_y component in the magnetic field.

B. Density of states and Bogoliubov Fermi surfaces

The DOS of proximitized holes exhibits a strong magnetic field anisotropy due to the very distinct behavior of hole spins under vertical or in-plane magnetic fields. For a given magnetic field, the DOS can be calculated as

$$\rho(E) = -\frac{1}{\pi} \int \text{Im Tr} \frac{1}{E + i0^+ - H_{\text{BdG}}} k dk d\phi_k, \quad (18)$$

integrating over the in-plane momentum. As previously noted, the in-plane magnetic field induces tilts to the spectrum depending on whether the Zeeman term is parallel to the Rashba field or not. By integrating the momentum orientation, we average out this behavior. Hence, under an in-plane magnetic field, the DOS shall give a qualitatively similar picture irrespective of the specific in-plane Zeeman orientation ϕ_B . In contrast, a vertical magnetic field is always perpendicular to the Rashba field for any value of ϕ_k . Therefore, the signatures in the DOS for vertical and in-plane magnetic fields provide different signatures.

In Fig. 7(a,b), we show the DOS as a function of vertical B_z and in-plane B_x magnetic fields at low $|\mu|$. As a function of B_z , Fig. 7(a), the DOS exhibits a series of peaks which are the van Hove singularities associated to the maxima in ϕ_k of the pairings $\Delta(k_3)$ and $\Delta(k_4)$. The black region in these plots illustrates the spectral gap, which decreases with increasing B_z , as expected from the previous analysis with magnetic fields. The different dependence on k of the two gaps leads to a non-trivial behavior of the van Hove singularities, which cross and swap places as a function of energy.

In contrast, in Fig. 7(b) we see many more features for the in-plane behavior of the DOS due to the spectrum

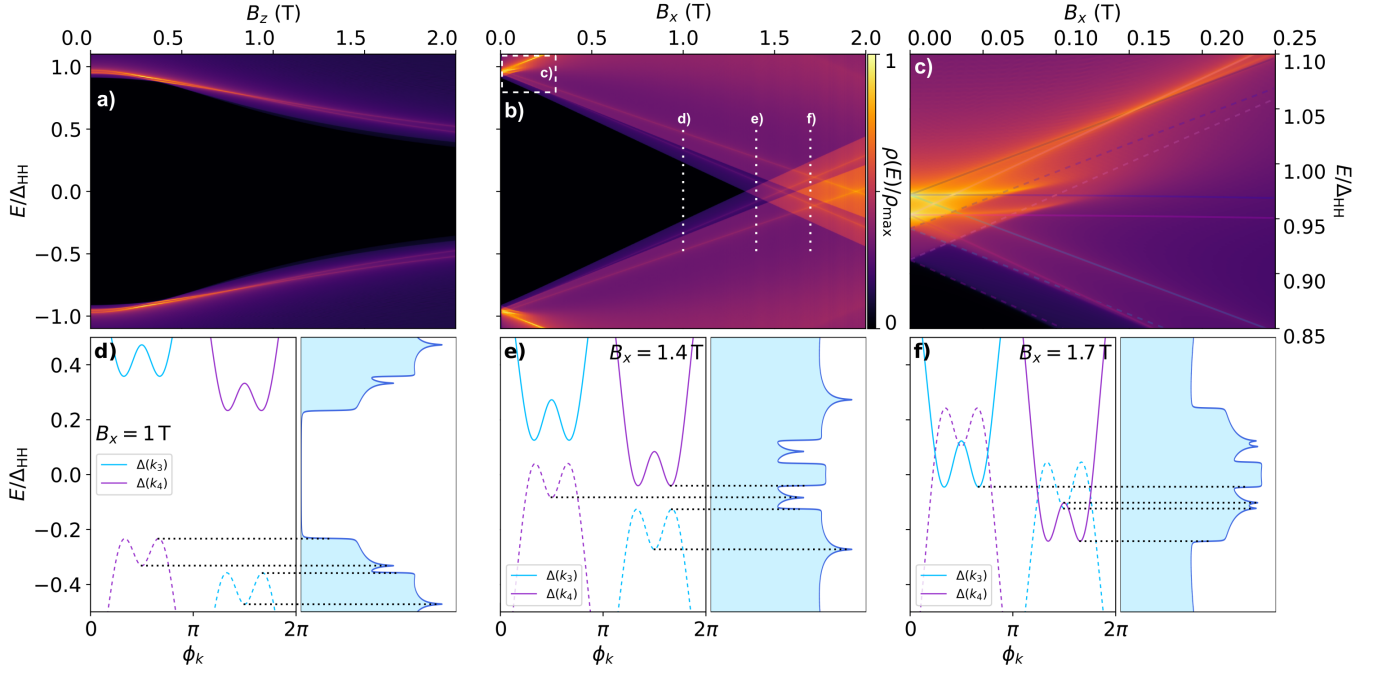


Figure 7. **DOS as a function of magnetic field.** (a) DOS centered around $E = 0$ as a function of the vertical magnetic field B_z with $\mu = -0.01$ eV. (b) DOS centered around $E = 0$ as a function of the in-plane magnetic field B_x . (c) DOS at low in-plane magnetic field, in the corresponding energy window marked in panel (b). (d-f) Hole band minima as a function of ϕ_k associated to $\Delta(k_3)$ and $\Delta(k_4)$ for the in-plane magnetic field marked with the corresponding dashed lines in panel (b), at (d) $B_x = 1$ T, (e) $B_x = 1.4$ T, and (f) $B_x = 1.7$ T. At their right, their corresponding cuts of the DOS. The black dashed lines relate the local minima and maxima with the different singularities in the DOS. Parameters: $\Delta_{\text{HH}} = 200 \mu\text{eV}$; $\mu = -0.01$ eV; $F = 0.5$ MV/m; Table I; Appendix D.

tilting. In this case, multiple van Hove singularities appear. The van Hove singularities are associated to newly emerging local maxima of the gap against ϕ_k for non-zero magnetic field, Figs. 7(d-f). Interestingly, as shown in Fig. 7(d), the anisotropic behavior with ϕ_k of the spin splitting δ_h in Eq. (14) introduce two local maxima at each anticrossing at $B_{\parallel} = 0$, leading to a couple of the van Hove singularities. These van Hove singularities split when $B_{\parallel} \neq 0$. A superconductor-semiconductor interface breaking cubic symmetry would introduce highly directional pairing terms treated in Sec. IV D and, therefore, break the symmetry between the two minima in each band, leading to measurable signatures in the DOS.

Importantly, as the in-plane Zeeman energy grows, the spectrum tilts linearly with B , reducing the gap as illustrated in Fig. 6(a). As can be seen in Fig. 7(b), the gap closes linearly with B . When the Zeeman energy parallel to the Rashba field $g_{zi}\mu_B B_{\parallel}$ surpasses the triplet pairing term at a given k_i , the gap closes at that value of k . An intermediate region emerges where only one of the two bands can get occupied since $\Delta(k_3)$ and $\Delta(k_4)$ exhibit different behavior with B as well. For sufficiently large in-plane magnetic fields, the gap closes and a finite DOS is observed at $E = 0$, see Figs. 7(e) and (f). In this case, the van Hove singularities from hole and time-reversed states converge to approximately the same

energy regions, giving rise to a more complex DOS with a diamond-like structure as a function of E and B_x in Fig. 7(b). Interestingly, this strong anisotropic behavior is already evident at low in-plane magnetic fields, see Fig. 7(c), where the van Hove singularities show an intricate behavior.

In Fig. 8 we focus on the behavior of these van Hove singularities. Despite the apparent complexity, the position of the peaks can be deduced from the competition between the Rashba-induced spin splitting δ_h and the Zeeman spin splitting related to the parallel g-factors g_{zx} and g_{zy} . δ_h has a $\cos 4\phi_k$ dependence coming from the cubic symmetry, leading to the two van Hove peaks per band at zero magnetic field in Fig. 8(b,c). When the magnetic field is turned on, the Zeeman field breaks the mirror symmetry around $\phi_k = n\pi$, leading to a splitting of the van Hove singularities. An intriguing case occurs when ϕ_k is such that the Zeeman energy for a given B_{\parallel} does not induce a tilt—the Zeeman term is perpendicular to the Rashba term—leaving a trace in the DOS as a van Hove singularity that remains invariant as a function of the amplitude $\|B\|$. This invariant singularity gets washed away for larger magnetic fields due to the deformation of the gap dependence with ϕ_k .

All the above predictions should constitute strong experimental signatures of a proximitized hole gas with

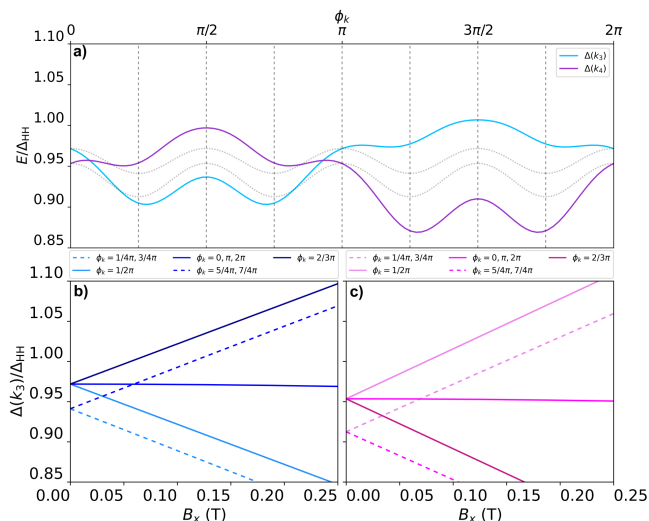


Figure 8. **Maxima, minima and van Hove singularities.** (a) Energy at k_3 and k_4 as a function of ϕ_k . While maxima and minima of the oscillations in both bands coincide at the same ϕ_k for $B = 0$ (grey dotted lines), this is no longer the case at finite in-plane magnetic field ($B_x = 0.07$ T in the plot) owing to the anisotropies discussed in the main text. This gives rise to the splittings in the energy positions of the van Hove singularities as a function of B_x (lower panels b and c) that are clearly seen in the DOS in Fig. 7c. Parameters: $\Delta_{\text{HH}} = 200 \mu\text{eV}$; $\mu = -0.01$ eV; $F = 0.5$ MV/m; Table I; Appendix D

large anisotropies and expected to appear in tunneling spectroscopy experiments, where the tunneling conductance is directly proportional to the DOS.

The anisotropic behavior of the gap against ϕ_k for in-plane magnetic fields is illustrated in Fig. 9 through Bogoliubov-Fermi surfaces [57, 58]. The points in k -space where the BdG bands cross the Fermi level form closed anisotropic surfaces, due to the anisotropic Rashba and Zeeman fields for holes. These Bogoliubov-Fermi surfaces are strongly dependent on the different parameters of the system. The orientation of the magnetic field ϕ_B leads to rotations of the surfaces in k -space. The distance between surfaces associated to the closure of different HH bands is related to the Rashba spin splitting, which is tunable through the electric field. Furthermore, by tuning the amplitude of the magnetic field, the shape and topology of the surfaces can be changed. These features are not unique to the low $|\mu|$ regime, and it is possible to show similar surfaces associated to four different bands for states with hybridized LH components. In this hybridized scenario, the value of Δ_{LH} further tunes the different surfaces, as can be seen in Fig. 9(c-d). Moreover, these surfaces illustrate the cubic symmetry as μ gets more negative, becoming less symmetric than the surfaces in Fig. 9(a-b) cases.

Experimentally, the emergence of such anisotropic

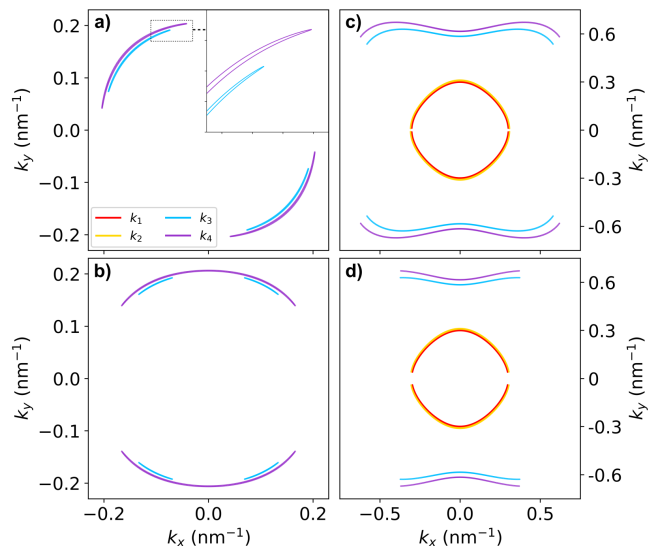


Figure 9. **Bogoliubov-Fermi bands.** (a-b) Bogoliubov-Fermi surfaces for $\mu = -0.01$ eV, $\|B\| = 1.7$ T, $\Delta_{\text{HH}} = 200 \mu\text{eV}$, with (a) $\phi_B = 0$, and (b) $\phi_B = \pi/4$. (c-d) Bogoliubov-Fermi surfaces for $\mu = -0.1$ eV, $B_x = 1.5$ T; with (c) $\Delta_{\text{LH}} = 0 \mu\text{eV}$, $\Delta_{\text{HH}} = 200 \mu\text{eV}$, and with (d) $\Delta_{\text{LH}} = 200 \mu\text{eV}$, $\Delta_{\text{HH}} = 0 \mu\text{eV}$. Parameters used: $F = 0.5$ MV/m (rest of parameters in Table I; Appendix D).

Bogoliubov-Fermi surfaces could be probed in a circuit QED setup. Specifically, the frequency of a resonant microwave circuit is expected to be modified by the contribution of the 2DHG to the kinetic inductance, which is inversely proportional to the superfluid density. This method has recently been demonstrated in a two-dimensional Al-InAs hybrid heterostructure [55].

VI. CONCLUSIONS

In this work, we have studied the proximity-induced superconductivity in a two-dimensional hole gas. We have found very rich anisotropic behavior in the inherited superconducting correlations for hole spins. We have distinguished two main regimes: at low $|\mu|$, only the bands with strong HH character at low k cross the Fermi level leading to a dominant pairing in the HH band; at μ below $-E_{hl}$ four different bands cross the Fermi level, including two bands with strong LH character at low k . We have considered pairing terms coming directly from the conduction band, HH band, and LH band, all of which exhibiting different dependencies with μ , which potentially allows to infer their contributions. The electron pairing through the conduction band induces both superconducting singlet and triplet correlations in the hole subspace. These contributions decrease as μ goes from the four-level regime to the low $|\mu|$ two-level and HH-dominated regime. In contrast, direct HH and LH pairing mechanisms induce triplet-only correlations at zero

magnetic field. In this case, a direct HH pairing mechanism leads to a maximal gap for low $|\mu|$ in the HH-like bands, while it increases with more negative μ for the LH-like bands. The opposite behavior occurs for a direct LH pairing amplitude. We have also considered disorder effects allowing mixed HH-LH pairing mechanisms. These introduce both singlet and triplet superconducting correlations in the hole subspace that decrease with μ , and rotate the pairings in k -space, reducing the overall symmetry of the gaps, potentially leading to extra singularities in DOS measurements. Overall, all different pairing mechanisms induce a non-trivial anisotropic k -dependence, in particular due to the cubic symmetry of the Ge crystal, which influences the singularities that are observed in DOS measurements.

When turning the magnetic field on, we have found strongly anisotropic behavior that can be experimentally tested. For vertical magnetic fields and low $|\mu|$ values, we find analogous behavior to proximitized Rashba nanowires where triplet and singlet pairing correlations are exchanged as B_z grows. The main difference with Rashba nanowires is the f-type superconductivity arising due to the cubic Rashba of holes. We have related the magnetic dependence to geometrical relationships with the g-factors of the hole spins. In contrast, when the magnetic field is in-plane, the component perpendicular to the Rashba field induces an identical behavior as with vertical magnetic fields in the pairing correlations with a reduced g-factor, while the component parallel to the Rashba field competes directly with the spin splitting inducing a tilt to the spectrum. Consequently, for sufficiently large in-plane magnetic fields, the gap may close at different points in k -space, forming non-trivial Bogoliubov-Fermi surfaces. In DOS measurements, this leads to a magnetic field value at which the gap closes and does not reopen, and where van Hove singularities coming from hole and time-reversed states converge in energy, giving rise to a diamond-like structure in the density of states. Note that the orbital corrections considered in Appendix G introduce strong g-factor renormalizations, particularly for vertical magnetic fields, which do not qualitatively change the analyzed behavior but quantitatively affect the values of magnetic field at which all these experimental signatures occur.

To conclude, after analyzing the wealth of possible pairings and anisotropies that can arise in a proximitized 2DHG, we believe that our model provides an excellent starting point for theoretical modeling of novel concepts and devices based on proximitized hole gases. In this context, systems of great current interest include superconducting spin qubits, subgap physics including Andreev and Shiba, minimal Kitaev chains and Majorana-based devices in general; as well as novel Josephson junctions including superconducting diodes. Given that so far most of the experiments with hybrid devices have been carried out on electron-based systems and that much of the experimental efforts are now directed towards holes,

we are confident that the new physics introduced in the latter, as yet almost unexplored, will undoubtedly enhance the palette of new phenomenologies and functionalities.

ACKNOWLEDGMENTS

Work supported by the Horizon Europe Framework Program of the European Commission through the European Innovation Council Pathfinder Grant No. 101115315 (QuKiT), the Spanish Comunidad de Madrid (CM) ‘‘Talento Program’’ (Project No. 2022-T1/IND-24070), the Fundaci3n General CSIC’s Com-Futuro programme under the Marie Sklodowska-Curie grant agreement No. 101034263 for EU Horizon 2020, the Spanish Ministry of Science, innovation, and Universities through Grants PID2021-125343NB-I00, RYC2022-037527-I, PID2022- 140552NA-I00, PID2023-148257NA-I00, and TED2021-130292B-C43 funded by MCIN/AEI/10.13039/501100011033, ‘‘ERDF A way of making Europe’’ and European Union Next Generation EU/PRTR. Support from the CSIC Interdisciplinary Thematic Platform (PTI+) on Quantum Technologies (PTI-QTEP+) is also acknowledged.

Note added. While finishing this manuscript, a preprint appeared in Arxiv [66] also addressing the theory of the Superconducting Proximity Effect in two-dimensional hole gases with partial overlap with our work.

Appendix A: 8KP Hamiltonian

Below we detail the explicit form of the different blocks appearing in the Hamiltonian (2), using the spinor basis $\Psi = (c_{1/2,\mathbf{k}}, c_{-1/2,\mathbf{k}}, b_{3/2,3/2,\mathbf{k}}, b_{3/2,1/2,\mathbf{k}}, b_{3/2,-1/2,\mathbf{k}}, b_{3/2,-3/2,\mathbf{k}}, b_{1/2,1/2,\mathbf{k}}, b_{1/2,-1/2,\mathbf{k}}, c_{1/2,-\mathbf{k}}, c_{-1/2,-\mathbf{k}}, b_{3/2,3/2,-\mathbf{k}}, b_{3/2,1/2,-\mathbf{k}}, b_{3/2,-1/2,-\mathbf{k}}, b_{3/2,-3/2,-\mathbf{k}}, b_{1/2,1/2,-\mathbf{k}}, b_{1/2,-1/2,-\mathbf{k}})^T$, where $c_{s_z,\mathbf{k}}$ ($b_{j,j_z\mathbf{k}}$) destroys an electron (hole) with angular momentum j , spin projection s_z (angular momentum projection j_z), and momentum \mathbf{k} . The standard blocks of conduc-

tion and valence bands and their coupling terms are:

$$H_{cb} = E_g + \frac{\hbar^2}{2m'}(k_x^2 + k_y^2 + k_z^2)$$

$$H_{cb-v} = \frac{P_{\text{Ge}}}{\sqrt{3}} \times \begin{pmatrix} -\sqrt{\frac{3}{2}}k_+ & \sqrt{2}k_z & \frac{1}{\sqrt{2}}k_- & 0 & -k_z & -k_- \\ 0 & -\frac{1}{\sqrt{2}}k_+ & \sqrt{2}k_z & \sqrt{\frac{3}{2}}k_- & -k_+ & k_z \end{pmatrix}$$

$$H_v = \begin{pmatrix} H_{4\text{KP}} & H_{8v-7v} \\ H_{8v-7v}^\dagger & H_{7v} \end{pmatrix}, \quad (\text{A1})$$

where $H_{4\text{KP}}$ is the Kohn-Luttinger Hamiltonian for LH and HH,

$$H_{4\text{KP}} = - \begin{pmatrix} P+Q & -S & R & 0 \\ -S^\dagger & P-Q & 0 & R \\ R^\dagger & 0 & P-Q & S \\ 0 & R^\dagger & S^\dagger & P+Q \end{pmatrix}$$

$$P = \frac{\hbar^2}{2m_0} \gamma'_1 (k_x^2 + k_y^2 + k_z^2) \quad (\text{A2})$$

$$Q = \frac{\hbar^2}{2m_0} \gamma'_2 (k_x^2 + k_y^2 - 2k_z^2)$$

$$R = \frac{\sqrt{3}\hbar^2}{2m_0} [-\gamma'_2 (k_x^2 - k_y^2) + 2i\gamma'_3 k_x k_y]$$

$$S = \frac{2\sqrt{3}\hbar^2}{2m_0} \gamma'_3 (k_x - ik_y)k_z,$$

and H_{7v} comprises the split-off valence band,

$$H_{7v} = -P - E_{\text{so}}$$

$$H_{8v-7v} = \begin{pmatrix} -\frac{1}{\sqrt{2}}S & \sqrt{2}R \\ -\sqrt{2}Q & \sqrt{\frac{3}{2}}S \\ \sqrt{\frac{3}{2}}S^* & \sqrt{2}Q \\ -\sqrt{2}R^* & -\frac{1}{\sqrt{2}}S^* \end{pmatrix}. \quad (\text{A3})$$

All the parameters needed for these Hamiltonians are tabulated and explained in Appendix B. We have also included a direct pairing potential induced to each band (Δ_{CB} , Δ_{LH} and Δ_{HH}) via contact with a superconductor, being

$$H_{cb}^\Delta = -i\sigma_y \Delta_{\text{CB}}$$

$$H_v^\Delta = \begin{pmatrix} 0 & 0 & 0 & \Delta_{\text{HH}} \\ 0 & 0 & \Delta_{\text{LH}} & 0 \\ 0 & -\Delta_{\text{LH}} & 0 & 0 \\ -\Delta_{\text{HH}} & 0 & 0 & 0 \end{pmatrix} \oplus 0_{2 \times 2}. \quad (\text{A4})$$

These pairings are assumed to be real without loss of generality.

Appendix B: Ge parameters for 8KP and 4KP models

Below we list the Ge band structure parameters for the 4KP model and their corrections for the 8KP model, extracted from [72].

E_g (eV)	0.8981
E_{so} (eV)	0.289
m_e^* (m_0)	0.041
γ_1	13.37
γ_2	4.23
γ_3	5.68
κ	3.41
q	0.06
P_{Ge} (eV · m ⁻¹)	$9.19 \cdot 10^{-10}$

Table I. Band structure parameters for Ge.

Note that these band parameters contain remote-band contributions of second order in k . Thus, for the 8KP model, we need to use reduced band parameters, subtracting the contributions of remote bands which are explicitly taken into account:

$$\frac{m_0}{m'} = \frac{m_0}{m_e^*} - \underbrace{\frac{2}{3} \frac{2m_0}{\hbar^2} \frac{P_{\text{Ge}}^2}{E_g}}_{\Gamma_{8v}} - \underbrace{\frac{1}{3} \frac{2m_0}{\hbar^2} \frac{P_{\text{Ge}}^2}{E_g + \Delta_0}}_{\Gamma_{7v}}$$

$$\gamma'_1 = \gamma_1 - \frac{1}{3} \frac{2m_0}{\hbar^2} \frac{P_{\text{Ge}}^2}{E_g}$$

$$\gamma'_{2,3} = \gamma_{2,3} - \frac{1}{6} \frac{2m_0}{\hbar^2} \frac{P_{\text{Ge}}^2}{E_g} \quad (\text{B1})$$

$$\kappa' = \kappa - \frac{1}{6} \frac{2m_0}{\hbar^2} \frac{P_{\text{Ge}}^2}{E_g}$$

$$\gamma_\Delta = \frac{2m_0 P_{\text{Ge}}^2}{3\hbar^2 E_g} = 7.38$$

Appendix C: Comparison of effective 4KP theory and the parent 8KP Hamiltonian

In Fig. C.1, we show a comparison between the effective 4KP and the original 8KP model for $H_v^\Delta = 0$, $H_c^\Delta = i\sigma_y \Delta_{\text{CB}}$ at $\theta_k = \pi/2$. In Fig. C.1(a,c) we show the position of the superconducting anticrossings $k_1(\phi_k)$ and $k_2(\phi_k)$. The effective model qualitatively captures the correct orientation dependence and only deviates from the parent Hamiltonian results in, roughly, a 15%. In Fig. C.1(b,d), we compare the magnitude of the anticrossings, resulting in an overall good agreement, except around $\phi_k = \pi/4$, which shows a factor 2 disagreement. The resulting error is mainly due to the lack of the split-off band, as illustrated when comparing the 4KP results with the 8KP for a decoupled split-off band (see light

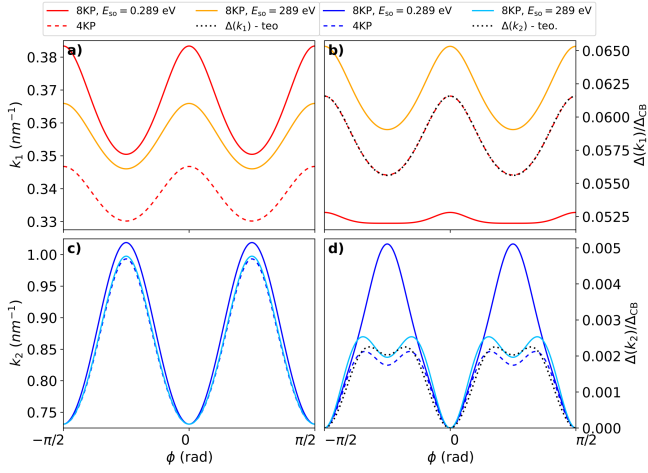


Figure C.1. **Comparison between 8KP and 4KP models.** (b,d) Gaps and (a,c) their positions in k , as a function of the spherical coordinate ϕ_k with $\theta_k = \pi/2$; at (a,b) $k_1(\phi_k, \pi/2, \mu)$ and (c,d) $k_2(\phi_k, \pi/2, \mu)$. Parameters used: $\Delta_{CB} = 200 \mu\text{eV}$; $\mu = -0.1 \text{ eV}$; Table I.

blue in Fig. C.1(d)). As noted previously, differences coming from the (lack of) split-off band lose relevance at the 2DHG regime for strained Ge, where most experiments take place.

Appendix D: Confinement along z direction

Assuming a vertical electric field F and hard infinite wall boundary conditions at $z = \pm L_W/2$, we find the following trial wave function for the ground-state Bastard wavefunction [63]

$$\psi_z(z, \beta) = \sqrt{\frac{4\beta(\pi^2 + \beta^2)}{\pi^2 L_W (1 - e^{-2\beta})}} \cos\left(\frac{\pi z}{L_W}\right) \times \exp\left[-\beta\left(\frac{z}{L_W} + \frac{1}{2}\right)\right] \quad (\text{D1})$$

The variational parameter β minimizes the ground-state energy of the vertical Hamiltonian

$$H_z = \frac{p_z^2}{2m_\perp} + eFz + V_{\text{barrier}}\theta_k\left(|z| - \frac{L_W}{2}\right) \quad (\text{D2})$$

where the barrier potential is approximated to a hard-wall condition $V_{\text{barrier}} \rightarrow \infty$, and m_\perp is the confinement mass along z , which is different for light and heavy holes,

$$m_\perp^L = \frac{m_0}{\gamma_1 + 2\gamma_2}, \quad m_\perp^H = \frac{m_0}{\gamma_1 - 2\gamma_2}. \quad (\text{D3})$$

Then, we compute the ground-state energy

$$E = \int_{-L_W/2}^{L_W/2} \psi_z(z, \beta) H_z \psi_z(z, \beta) dz = FL_W \left(\frac{1}{2\beta} + \frac{\beta}{\pi^2 + \beta^2} - \frac{1}{2} \coth \beta \right) + \frac{\hbar^2(\pi^2 + \beta^2)}{2m_\perp L_W^2} \quad (\text{D4})$$

and we minimize this quantity to (numerically) obtain a $\beta_{L,H}$ such that $\partial_\beta E = 0$ for each m_\perp^L and m_\perp^H . Now, we extract the following quantities,

$$\begin{aligned} \langle p_z^2 \rangle_H &= \langle 0_H | p_z^2 | 0_H \rangle = \frac{\hbar^2}{L_W^2} (\pi^2 + \beta_H^2) \\ \langle p_z^2 \rangle_L &= \langle 0_L | p_z^2 | 0_L \rangle = \frac{\hbar^2}{L_W^2} (\pi^2 + \beta_L^2) \\ E_{hl} &= E_{hl}^{(\text{strain})} + \frac{\hbar^2(\pi^2 + \beta_L^2)}{2m_\perp^L L_W^2} - \frac{\hbar^2(\pi^2 + \beta_H^2)}{2m_\perp^H L_W^2} \\ \mathcal{O}_0 &= \langle 0_H | 0_L \rangle = \frac{4(e^{\bar{\beta}} - 1)\tilde{K}}{\bar{\beta}(4\pi^2 + \bar{\beta}^2)} \\ \alpha_0 &= -i \langle 0_H | p_z | 0_L \rangle = \frac{2\hbar(\beta_L - \beta_H)(e^{\bar{\beta}} - 1)\tilde{K}}{L_W \bar{\beta}(4\pi^2 + \bar{\beta}^2)} \\ z_0 &= \langle 0_H | z | 0_L \rangle = -\frac{4L_W \tilde{K} e^{\bar{\beta}/2}}{\bar{\beta}^2(4\pi^2 + \bar{\beta}^2)^2} \\ &\quad \times [\bar{\beta}(\bar{\beta}^2 + 4\pi^2) \cosh(\bar{\beta}/2) - 2(3\bar{\beta}^2 + 4\pi^2) \sinh(\bar{\beta}/2)] \\ \tilde{K} &= \prod_{\alpha=H,L} \sqrt{\beta_\alpha(\pi^2 + \beta_\alpha^2)(\coth \beta_\alpha - 1)} \\ \bar{\beta} &= \beta_H + \beta_L \end{aligned} \quad (\text{D5})$$

where the expectation values are integrated in the interval $z \in [-L_W/2, L_W/2]$.

Appendix E: Exact diagonalization of the 4-bands Hamiltonian

By projecting to the ground state of the vertical motion in the 2DHG and assuming $B = 0$, it is possible to analytically diagonalize the 4-band Kohn-Luttinger Hamiltonian in Eq. (A2) and obtain exact analytical expressions for the pairing terms. When projecting to the vertical ground state, the expected value of $\langle 0_H | p_z | 0_L \rangle$ is an imaginary quantity, see Eq. (D5), transforming the terms that go with S in Eq. (A2) into an effective k-dependent Zeeman interaction. The diagonalization procedure consists on the concatenation of different block-diagonalizations. The first step is to define a mixing angle θ_R between states $|3/2, \pm 3/2\rangle$ and $|3/2, \mp 1/2\rangle$, respectively:

$$\begin{aligned} \Omega_{RQ} &= \sqrt{(-E_{hl} + Q)^2 + |R|^2} \\ \theta_R &= -\arcsin\left(\frac{R \exp(-i\phi_R)}{\Omega_{RQ}}\right), \end{aligned} \quad (\text{E1})$$

where ϕ_R is the phase of the R term, such that $R = \Omega_{RQ} \sin \theta_R e^{i\phi_R}$ and $Q = \frac{E\hbar t}{2} + \Omega_{RQ} \cos \theta_R$. From here, we diagonalize the $|3/2, \pm 3/2\rangle$ - $|3/2, \mp 1/2\rangle$ blocks with an unitary U_1 , arriving at

$$H_{4KP}^{(1)} = U_1 H_{4KP} U_1^\dagger = -P - \mu + \begin{pmatrix} -\Omega_{RQ} & S^* \sin \theta_R & 0 & S^* \cos \theta_R \\ S \sin \theta_R & -\Omega_{RQ} & -S \cos \theta_R & 0 \\ 0 & -S^* \cos \theta_R & \Omega_{RQ} & S^* \sin \theta_R \\ S \cos \theta_R & 0 & S \sin \theta_R & \Omega_{RQ} \end{pmatrix}. \quad (\text{E2})$$

The next step is to diagonalize the blocks connected by $\cos \theta_R$. We define here the mixing angle θ_S , such that

$$\Omega_{SRQ} = \sqrt{(\Omega_{RQ}^2 + |S|^2 \cos^2 \theta_R)} \\ \theta_S = -\arcsin\left(\frac{S \cos \theta_R \exp(-i\phi_S)}{\Omega_{SRQ}}\right), \quad (\text{E3})$$

where ϕ_S is the imaginary phase of S , analogously to ϕ_R and R . Note that S has been projected to the vertical ground state. We end up with

$$H_{4KP}^{(2)} = U_2 H_{4KP}^{(1)} U_2^\dagger = -P - \mu + \Omega_{SRQ} \times \begin{pmatrix} -1 & -h_1 e^{i\phi_S} & 0 & h_2 e^{i\phi_S} \\ -h_1 e^{-i\phi_S} & -1 & h_2 e^{-i\phi_S} & 0 \\ 0 & h_2 e^{i\phi_S} & 1 & h_1 e^{i\phi_S} \\ h_2 e^{-i\phi_S} & 0 & h_1 e^{-i\phi_S} & 1 \end{pmatrix}, \quad (\text{E4})$$

where $h_1 = \cos \theta_S \sin \theta_S \tan \theta_R$ and $h_2 = \sin^2 \theta_S \tan \theta_R$. The next step is to rotate the blocks with same diagonal

terms with unitary U_3 . This leaves only the anti-diagonal that goes with h_2 as the only non-diagonal terms. To finish the diagonalization, we define the following terms

$$\Omega_{\pm} = \Omega_{SRQ} \sqrt{\sin^4 \theta_S \tan^2 \theta_{RQ} + (\cos \theta_S \sin \theta_S \tan \theta_R \pm 1)^2} \\ \theta_{\pm} = \arcsin\left(\frac{\Omega_{SRQ} \sin^2 \theta_S \tan \theta_R}{\Omega_{\pm}}\right), \quad (\text{E5})$$

where the mixing angles θ_{\pm} are not fully independent. However, using these mixing angles to perform the final rotation U_4 , leads to a full diagonal form:

$$H_{4KP}^{(diag)} = U_4 U_3 U_2 U_1 H_{4KP} U_1^\dagger U_2^\dagger U_3^\dagger U_4^\dagger = -P - \mu + \text{diag}(+\Omega_-, -\Omega_-, +\Omega_+, -\Omega_+). \quad (\text{E6})$$

1. Exact expressions for the pairing terms

The exact diagonalization of the time-reversed terms follows an identical reasoning. Let $U = U_4 U_3 U_2 U_1$ and $U' = U'_4 U'_3 U'_2 U'_1$, with U'_i being the time-reversed equivalent of U_i , any pairing Hamiltonian within the valence band $H_{v,j}^\Delta$ becomes

$$H_{v,j}^{\Delta(d)} = U H_{v,j}^\Delta U'^\dagger, \quad (\text{E7})$$

this equation allows us to extract exact analytical expressions of the pairings, valid at all orders. For the non-zero conduction band pairing terms, we get

$$\frac{\tilde{\Delta}_{l,0}^{(c)}}{\Delta_{CB}} = \frac{\tilde{\Delta}_{h,0}^{(c)}}{\Delta_{CB}} = \frac{e^{-i(2\phi_R + \phi_S)}}{E_g - 2\mu} \left[\sin\left(\frac{\theta_-}{2} - \frac{\theta_+}{2} + \theta_S\right) \left(R_\Delta \cos\left(\frac{\theta_-}{2} + \frac{\theta_+}{2} - \theta_R\right) + Q_\Delta e^{i\phi_R} \sin\left(\frac{\theta_-}{2} + \frac{\theta_+}{2} - \theta_R\right) \right) \right] \\ \frac{\tilde{\Delta}_{l,x}^{(c)}}{\Delta_{CB}} = \frac{\tilde{\Delta}_{h,x}^{(c)}}{\Delta_{CB}} = \frac{S_\Delta e^{-i(\phi_R + 2\phi_S)} \sin\left(\frac{\theta_-}{2} + \frac{\theta_+}{2} - \theta_R\right)}{E_g - 2\mu} \\ \frac{\tilde{\Delta}_{l,z}^{(c)}}{\Delta_{CB}} = \frac{e^{-i(2\phi_R + \phi_S)}}{E_g - 2\mu} \left[\cos\left(\frac{\theta_-}{2} - \frac{\theta_+}{2} + \theta_S\right) \left(-R_\Delta \sin(\theta_-/2 + \theta_+/2 - \theta_R) + Q_\Delta e^{i\phi_R} \cos(\theta_-/2 + \theta_+/2 - \theta_R) \right) - P_\Delta e^{i\phi_R} \right] \\ \frac{\tilde{\Delta}_{h,z}^{(c)}}{\Delta_{CB}} = -\frac{e^{-i(2\phi_R + \phi_S)}}{E_g - 2\mu} \left[\cos\left(\frac{\theta_-}{2} - \frac{\theta_+}{2} + \theta_S\right) \left(-R_\Delta \sin(\theta_-/2 + \theta_+/2 - \theta_R) + Q_\Delta e^{i\phi_R} \cos(\theta_-/2 + \theta_+/2 - \theta_R) \right) + P_\Delta e^{i\phi_R} \right]. \quad (\text{E8})$$

For the direct HH and LH we define $\bar{\Delta}_H = (\Delta_{HH} + \Delta_{LH})/2$ and $\Delta_{H-} = \Delta_{HH} - \Delta_{LH}$, and the non-zero pairing terms are

$$\frac{\tilde{\Delta}_{l,0}^{(v)}}{\bar{\Delta}_H} = \frac{\tilde{\Delta}_{h,0}^{(v)}}{\bar{\Delta}_H} = \frac{1}{2} e^{-i(\phi_R + \phi_S)} (\cos(\theta_+ - \theta_R - \theta_S) - \cos(\theta_- - \theta_R + \theta_S)) \\ \tilde{\Delta}_{l,z}^{(v)} = \frac{1}{2} e^{-i(\phi_R + \phi_S)} [\Delta_{H-} - \bar{\Delta}_H (\cos(\theta_- - \theta_R + \theta_S) + \cos(\theta_+ - \theta_R - \theta_S))] \\ \tilde{\Delta}_{h,z}^{(v)} = \frac{1}{2} e^{-i(\phi_R + \phi_S)} [\Delta_{H-} + \bar{\Delta}_H (\cos(\theta_- - \theta_R + \theta_S) + \cos(\theta_+ - \theta_R - \theta_S))]. \quad (\text{E9})$$

Finally, the mixed terms are

$$\begin{aligned}
\frac{\tilde{\Delta}_{l,0}^{(m)}}{\Delta_R} &= \frac{\tilde{\Delta}_{h,0}^{(m)}}{\Delta_R} = e^{-i(\phi_R+\phi_S)} \cos\left(\theta_R - \frac{\theta_-}{2} - \frac{\theta_+}{2}\right) \sin\left(\theta_S + \frac{\theta_-}{2} - \frac{\theta_+}{2}\right) \cos(\phi_R - \chi_R) \\
\frac{\tilde{\Delta}_{l,x}^{(m)}}{\Delta_R} &= -\frac{\tilde{\Delta}_{h,x}^{(m)}}{\Delta_R} = -ie^{-i(\phi_R+\phi_S)} \sin\left(\frac{\theta_-}{2} - \frac{\theta_+}{2} + \theta_S\right) \sin(\phi_R - \chi_R) \\
\frac{\tilde{\Delta}_{l,y}^{(m)}}{\Delta_S} &= -\frac{\tilde{\Delta}_{h,y}^{(m)}}{\Delta_S} = ie^{-i(\phi_R+\phi_S)} \sin\left(\frac{\theta_-}{2} - \frac{\theta_+}{2} + \theta_S\right) \cos(\phi_S - \chi_S) \\
\frac{\tilde{\Delta}_{l,z}^{(m)}}{\Delta_R} &= -\frac{\tilde{\Delta}_{h,z}^{(m)}}{\Delta_R} = -e^{-i(\phi_R+\phi_S)} \sin\left(\theta_R - \frac{\theta_-}{2} - \frac{\theta_+}{2}\right) \cos\left(\theta_S + \frac{\theta_-}{2} - \frac{\theta_+}{2}\right) \cos(\phi_R - \chi_R).
\end{aligned} \tag{E10}$$

Appendix F: Rotation of the singlet and triplet pairing terms for a general magnetic field

Given the Zeeman Hamiltonian given in Eq. (15), the Larmor vectors of hole and their time-reversed partners are given by:

$$\begin{aligned}
\boldsymbol{\omega}_L &= (g_{xz}B_z, g_{yx}B_x + g_{yy}B_y, \frac{\delta_h}{\mu_B} + g_{zx}B_x + g_{zy}B_y) \\
\bar{\boldsymbol{\omega}}_L &= -(g_{xz}B_z, g_{yx}B_x + g_{yy}B_y, \frac{\delta_h}{\mu_B} - g_{zx}B_x - g_{zy}B_y),
\end{aligned} \tag{F1}$$

such that $(\mu_B/2)\boldsymbol{\omega}_L \cdot \boldsymbol{\sigma}$ and $(\mu_B/2)\bar{\boldsymbol{\omega}}_L \cdot \boldsymbol{\sigma}$ are the effective Zeeman terms in each subspace. To understand how the pairing terms transform in the eigenbasis, we need to diagonalize the spin-splitting terms. For this purpose, we define the angles Θ and $\bar{\Theta}$ as the deviation angles from the z and $-z$ axis, respectively:

$$\begin{aligned}
\Theta &= \arccos\left(\frac{\omega_L^{(z)}}{\|\boldsymbol{\omega}_L\|}\right) \\
\bar{\Theta} &= \arccos\left(-\frac{\bar{\omega}_L^{(z)}}{\|\bar{\boldsymbol{\omega}}_L\|}\right).
\end{aligned} \tag{F2}$$

Furthermore, we define a normalized rotation axis given by the perpendicular between $\boldsymbol{\omega}_L$ and the z axis:

$$\mathbf{n} = \frac{\boldsymbol{\omega}_L \times \hat{z}}{\|\boldsymbol{\omega}_L\|}, \tag{F3}$$

while generally $\mathbf{n} \neq \bar{\mathbf{n}}$, the choice of $\bar{\Theta}_k$ and basis set leads to the same rotation axis for the time-reversed sector $\mathbf{n} = \bar{\mathbf{n}}$. The rotations that bring hole and time-reversed Hamiltonians to diagonal form are given by $R = \exp(i\Theta \mathbf{n} \cdot \boldsymbol{\sigma}/2)$ and $\bar{R} = \exp(i\bar{\Theta} \mathbf{n} \cdot \boldsymbol{\sigma}/2)$. Defining $\Theta_{\pm} = (\Theta \pm \bar{\Theta})/2$ and given a general pairing term of the form $\Delta_0 \sigma_0 + \boldsymbol{\Delta} \cdot \boldsymbol{\sigma}$, the rotated term becomes

$$\begin{aligned}
R(\Delta_0 \sigma_0) \bar{R}^\dagger &= \Delta_0 [\cos \Theta_- \sigma_0 + i \sin \Theta_- \mathbf{n} \cdot \boldsymbol{\sigma}] \\
R(\boldsymbol{\Delta} \cdot \boldsymbol{\sigma}) \bar{R}^\dagger &= \cos \Theta_+ \mathbf{n} \times (\boldsymbol{\Delta} \times \mathbf{n}) \cdot \boldsymbol{\sigma} - \sin \Theta_+ (\mathbf{n} \times \boldsymbol{\Delta}) \cdot \boldsymbol{\sigma} \\
&\quad + (\mathbf{n} \cdot \boldsymbol{\Delta}) [\cos \Theta_- (\mathbf{n} \cdot \boldsymbol{\sigma}) + i \sin \Theta_- \sigma_0],
\end{aligned} \tag{F4}$$

which indicates in a general manner the geometrical relationships between singlet and triplet pairings with the imbalance of the Zeeman and Rashba spin-splittings.

Appendix G: Magneto-orbital corrections

The magnetic response of hole spins is known to be heavily influenced by the vector potential [71]. We estimate corrections to the proximitized hole Hamiltonian arising due to the vector potential. In the Kohn-Luttinger Hamiltonian, the vector potential \mathbf{A} can be included through the minimal coupling $\mathbf{p} \rightarrow \boldsymbol{\Pi} = \mathbf{p} + e\mathbf{A}$. Given a choice of gauge, the vector potential acquires a position dependence, and the momenta can no longer be treated as a good quantum number anymore. In this scenario, exact diagonalization of the Kohn-Luttinger Hamiltonian is not possible, hence, we focus on the perturbative regime of HHs at low $|\mu|$. For considering magneto-orbital effects we perform quasi-degenerate perturbation theory [24, 36] to integrate out the contributions from the conduction and light-hole bands to the heavy-hole manifold.

The effective HH 2DHG Hamiltonian in the presence of orbital effects can be estimated to be:

$$\begin{aligned}
H_{HH}^{(0)} &= \frac{1}{2m_{\parallel}} (\Pi_x^2 + \Pi_y^2) + \frac{\mu_B}{2} \boldsymbol{\sigma} \cdot g(\boldsymbol{\Pi}) \cdot \mathbf{B} - i\alpha_{\square} \Pi_-^3 \sigma_- \\
&\quad - i\alpha_{\square} \Pi_+ \Pi_- \Pi_+ \sigma_- - \mu + h.c.,
\end{aligned} \tag{G1}$$

where m_{\parallel} is the effective in-plane effective mass of heavy-holes, $\Pi_{\pm} = (\Pi_x \pm i\Pi_y)$ and α_{\square} , and α_{\circ} are spherical and cubic Rashba coefficients:

$$\begin{aligned}
\alpha_{\circ} &= \frac{3\alpha_0 \gamma_3 (\gamma_2 + \gamma_3) \mathcal{O}}{2E_{hl} m_0^2} \\
\alpha_{\square} &= \frac{3\alpha_0 \gamma_3 (\gamma_2 - \gamma_3) \mathcal{O}}{2E_{hl} m_0^2}.
\end{aligned} \tag{G2}$$

It is important to note that perturbative results in Eq. (G1) are not given in the Rashba eigenbasis used

for prior results. The main corrections are a renormalization of the g-factors:

$$\begin{aligned}
g_{xx} &= 3q + (\lambda\Pi_x^2 - \lambda'\Pi_y^2) \\
g_{yy} &= -3q - (\lambda\Pi_y^2 - \lambda'\Pi_x^2) \\
g_{xy} &= -g_{yx} = \lambda_{xy}\{\Pi_x, \Pi_y\} \\
g_{zz} &= 6\kappa + \frac{27}{2}q - 2\gamma_h,
\end{aligned} \tag{G3}$$

where $\{A, B\} = (AB + BA)/2$, and λ , λ' , λ_{xy} , and γ_h are parameters characterizing the perturbative corrections to the g-factors.

$$\begin{aligned}
\lambda &= \frac{6}{\hbar m_0 E_{hl}} (4\gamma_3^2 \alpha_0 z_0 + \hbar\gamma_2 \kappa \mathcal{O}^2) \\
\lambda' &= \frac{6\gamma_2}{\hbar m_0 E_{hl}} (4\gamma_3 \alpha_0 z_0 + \hbar\kappa \mathcal{O}^2). \\
\lambda_{xy} &= \frac{6\gamma_3}{\hbar m_0 E_{hl}} (2(\gamma_2 + \gamma_3) \alpha_0 z_0 + \hbar\kappa \mathcal{O}^2).
\end{aligned} \tag{G4}$$

In particular, we get a strong correction to the vertical g factor, which can go from $g_{zz} \approx 21$ without \mathbf{A} to $g_{zz} \approx 13$ when considering \mathbf{A} . Comparing with the g-factors in the Rashba eigenbasis from Eq. (16), we expect the g_{xz} term to acquire such correction. In addition, we get a correc-

tion $\lambda \neq \lambda'$, which prevents cancellation of the perturbative correction for $k_x = k_y$ of the in-plane g-factors g_{xx} and g_{yy} , which is equivalent to a small renormalization of the parameters and angular dependence in the in-plane g-factors of Eq. (16). Therefore, we expect quantitative corrections to the observables, such as a small renormalization of how fast the bands tilt with in-plane magnetic fields and a lower dependence on the vertical magnetic field for the triplet pairing, as given in Fig. 6(c,f).

Strikingly, orbital corrections to the pairing terms are negligible to linear order in the magnetic field, with only quadratic corrections becoming relevant. Perturbatively, the contribution to the pairings coming from holes with \mathbf{k} gets canceled out exactly with the contribution from their time-reversed states with $-\mathbf{k}$. Hence, only at large magnetic fields the pairing terms get quadratic magnetic corrections. For instance, using $\Pi_i^* = \Pi_i(-k)$, the pairing terms from the conduction band in Eq. (5) become:

$$\begin{aligned}
P_\Delta &= \frac{1}{2m_0} \gamma_\Delta (\Pi_x \Pi_x^* + \Pi_y \Pi_y^* + \Pi_z \Pi_z^* + i\Pi_x \Pi_y^* - \Pi_y \Pi_x^*) \\
Q_\Delta &= \frac{1}{4m_0} \gamma_\Delta (\Pi_x \Pi_x^* + \Pi_y \Pi_y^* - 2\Pi_z \Pi_z^* + i\Pi_x \Pi_y^* - \Pi_y \Pi_x^*) \\
R_\Delta &= \frac{1}{4m_0} \sqrt{3} [-\gamma_\Delta (\Pi_x \Pi_x^* - \Pi_y \Pi_y^*) + i\gamma_\Delta (\Pi_x \Pi_y^* + \Pi_y \Pi_x^*)] \\
S_\Delta &= \frac{1}{2m_0} \sqrt{3} \gamma_\Delta \Pi_- \Pi_z^*.
\end{aligned} \tag{G5}$$

-
- [1] J. Alicea, New directions in the pursuit of majorana fermions in solid state systems, *Rep. Prog. Phys.* **75**, 076501 (2012).
- [2] M. Leijnse and K. Flensberg, Introduction to topological superconductivity and Majorana fermions, **27**, 124003 (2012).
- [3] R. Aguado, *La Rivista del Nuovo Cimento* **40**, 523 (2017).
- [4] R. M. Lutchyn, E. P. A. M. Bakkers, L. P. Kouwenhoven, P. Krogstrup, C. M. Marcus, and Y. Oreg, *Nature Review Materials* **3**, 52 (2018).
- [5] E. Prada, P. San-Jose, M. W. A. de Moor, A. Geresdi, E. J. H. Lee, J. Klinovaja, D. Loss, J. Nygård, R. Aguado, and L. P. Kouwenhoven, From andreev to majorana bound states in hybrid superconductor-semiconductor nanowires, *Nat. Rev. Phys.* **2**, 575 (2020).
- [6] R. Aguado and L. P. Kouwenhoven, Majorana qubits for topological quantum computing, *Physics Today* **73**, 44 (2020).
- [7] K. Flensberg, F. von Oppen, and A. Stern, Engineered platforms for topological superconductivity and majorana zero modes, *Nat. Rev. Mat.* **6**, 944 (2021).
- [8] R. Aguado, A perspective on semiconductor-based superconducting qubits, *Applied Physics Letters* **117**, 240501 (2020).
- [9] R. Seoane Souto and R. Aguado, *Subgap States in Semiconductor-Superconductor Devices for Quantum Technologies: Andreev Qubits and Minimal Majorana Chains*, chapter 3 in *New Trends and Platforms for Quantum Technologies*, edited by R. Aguado, R. Citro, M. Lewenstein, and M. Stern (Springer Nature Switzerland, Cham, 2024) pp. 133–223.
- [10] G. Burkard, T. D. Ladd, A. Pan, J. M. Nichol, and J. R. Petta, Semiconductor spin qubits, *Reviews of Modern Physics* **95**, 025003 (2023).
- [11] W. Huang, C. Yang, K. Chan, T. Tanttu, B. Hensen, R. Leon, M. Fogarty, J. Hwang, F. Hudson, K. M. Itoh, *et al.*, Fidelity benchmarks for two-qubit gates in silicon, *Nature* **569**, 532 (2019).
- [12] A. Noiri, K. Takeda, T. Nakajima, T. Kobayashi, A. Sammak, G. Scappucci, and S. Tarucha, Fast universal quantum gate above the fault-tolerance threshold in silicon, *Nature* **601**, 338 (2022).
- [13] A. R. Mills, C. R. Guinn, M. J. Gullans, A. J. Sigillito, M. M. Feldman, E. Nielsen, and J. R. Petta, Two-qubit silicon quantum processor with operation fidelity exceeding 99%, *Science Advances* **8**, eabn5130 (2022).
- [14] X. Xue, T. Watson, J. Helsen, D. R. Ward, D. E. Savage, M. G. Lagally, S. N. Coppersmith, M. Eriksson, S. Wehner, and L. M. Vandersypen, Benchmarking gate fidelities in a si/sige two-qubit device, *Physical Review X* **9**, 021011 (2019).
- [15] A. Blais, A. L. Grimsmo, S. M. Girvin, and A. Wallraff, Circuit quantum electrodynamics, *Reviews of Modern Physics* **93**, 025005 (2021).
- [16] M. Hays, V. Fatemi, D. Bouman, J. Cerrillo, S. Diamond,

- K. Serniak, T. Connolly, P. Krogstrup, J. Nygård, A. L. Yeyati, A. Geresdi, and M. H. Devoret, Coherent manipulation of an andreev spin qubit, *Science* **373**, 430 (2021).
- [17] M. Pita-Vidal, A. Bargerbos, R. Žitko, L. J. Splitthoff, L. Grünhaupt, J. J. Wesdorp, Y. Liu, L. P. Kouwenhoven, R. Aguado, B. van Heck, A. Kou, and C. K. Andersen, Direct manipulation of a superconducting spin qubit strongly coupled to a transmon qubit, *Nature Physics* **19**, 1110 (2023).
- [18] E. J. H. Lee, X. Jiang, M. Houzet, R. Aguado, C. M. Lieber, and S. De Franceschi, Spin-resolved andreev levels and parity crossings in hybrid superconductor–semiconductor nanostructures, *Nature Nanotechnology* **9**, 79 (2014).
- [19] C. Janvier, L. Tosi, L. Bretheau, Ç. Ö. Girit, M. Stern, P. Bertet, P. Joyez, D. Vion, D. Esteve, M. F. Goffman, H. Pothier, and C. Urbina, Coherent manipulation of andreev states in superconducting atomic contacts, *Science* **349**, 1199 (2015).
- [20] M. Hays, V. Fatemi, K. Serniak, D. Bouman, S. Diamond, G. de Lange, P. Krogstrup, J. Nygård, A. Geresdi, and M. H. Devoret, Continuous monitoring of a trapped superconducting spin, *Nature Physics* **16**, 1103 (2020).
- [21] A. Bargerbos, M. Pita-Vidal, R. Žitko, J. Ávila, L. J. Splitthoff, L. Grünhaupt, J. J. Wesdorp, C. K. Andersen, Y. Liu, L. P. Kouwenhoven, R. Aguado, A. Kou, and B. van Heck, Singlet-doublet transitions of a quantum dot josephson junction detected in a transmon circuit, *PRX Quantum* **3**, 030311 (2022).
- [22] A. Bargerbos, M. Pita-Vidal, R. Žitko, L. J. Splitthoff, L. Grünhaupt, J. J. Wesdorp, Y. Liu, L. P. Kouwenhoven, R. Aguado, C. K. Andersen, A. Kou, and B. van Heck, Spectroscopy of spin-split andreev levels in a quantum dot with superconducting leads, *Phys. Rev. Lett.* **131**, 097001 (2023).
- [23] A. Dimoulas, P. Tsipas, A. Sotiropoulos, and E. Evangelou, Fermi-level pinning and charge neutrality level in germanium, *Applied physics letters* **89**, 10.1063/1.2410241 (2006).
- [24] R. Winkler, *Spin-orbit coupling effects in two-dimensional electron and hole systems*, Springer tracts in modern physics (Springer, Berlin, 2003).
- [25] P. Philippopoulos, S. Chesi, D. Culcer, and W. Coish, Pseudospin-electric coupling for holes beyond the envelope-function approximation, *Physical Review B* **102**, 075310 (2020).
- [26] Y. Liu, J.-X. Xiong, Z. Wang, W.-L. Ma, S. Guan, J.-W. Luo, and S.-S. Li, Emergent linear rashba spin-orbit coupling offers fast manipulation of hole-spin qubits in germanium, *Physical Review B* **105**, 075313 (2022).
- [27] E. A. Rodríguez-Mena, J. C. Abadillo-Uriel, G. Veste, B. Martinez, J. Li, B. Sklénard, and Y.-M. Niquet, Linear-in-momentum spin orbit interactions in planar ge/gesi heterostructures and spin qubits, *Physical Review B* **108**, 205416 (2023).
- [28] A. Crippa, R. Maurand, L. Bourdet, D. Kotekar-Patil, A. Amisse, X. Jehl, M. Sanquer, R. Laviéville, H. Bohuslavskiy, L. Hutin, *et al.*, Electrical spin driving by g-matrix modulation in spin-orbit qubits, *Physical review letters* **120**, 137702 (2018).
- [29] V. P. Michal, B. Venitucci, and Y.-M. Niquet, Longitudinal and transverse electric field manipulation of hole spin-orbit qubits in one-dimensional channels, *Physical Review B* **103**, 045305 (2021).
- [30] L. Terrazos, E. Marcellina, Z. Wang, S. Coppersmith, M. Friesen, A. Hamilton, X. Hu, B. Koiller, A. Saraiva, D. Culcer, *et al.*, Theory of hole-spin qubits in strained germanium quantum dots, *Physical Review B* **103**, 125201 (2021).
- [31] T. Zhang, H. Liu, F. Gao, G. Xu, K. Wang, X. Zhang, G. Cao, T. Wang, J. Zhang, X. Hu, *et al.*, Anisotropic g-factor and spin-orbit field in a germanium hut wire double quantum dot, *Nano Letters* **21**, 3835 (2021).
- [32] F. N. Froning, L. C. Camenzind, O. A. van der Molen, A. Li, E. P. Bakkers, D. M. Zumbühl, and F. R. Braakman, Ultrafast hole spin qubit with gate-tunable spin-orbit switch functionality, *Nature Nanotechnology* **16**, 308 (2021).
- [33] S. Liles, F. Martins, D. Miserev, A. Kiselev, I. Thorvaldson, M. Rendell, I. Jin, F. Hudson, M. Veldhorst, K. Itoh, *et al.*, Electrical control of the g tensor of the first hole in a silicon mos quantum dot, *Physical Review B* **104**, 235303 (2021).
- [34] B. Martinez, J. C. Abadillo-Uriel, E. A. Rodríguez-Mena, and Y.-M. Niquet, Hole spin manipulation in inhomogeneous and nonseparable electric fields, *Physical Review B* **106**, 235426 (2022).
- [35] D. Jirovec, P. M. Mutter, A. Hofmann, A. Crippa, M. Rychetsky, D. L. Craig, J. Kukucka, F. Martins, A. Ballabio, N. Ares, *et al.*, Dynamics of hole singlet-triplet qubits with large g-factor differences, *Physical Review Letters* **128**, 126803 (2022).
- [36] J. C. Abadillo-Uriel, E. A. Rodríguez-Mena, B. Martinez, and Y.-M. Niquet, Hole-spin driving by strain-induced spin-orbit interactions, *Physical Review Letters* **131**, 097002 (2023).
- [37] R. Maurand, X. Jehl, D. Kotekar-Patil, A. Corna, H. Bohuslavskiy, R. Laviéville, L. Hutin, S. Barraud, M. Vinet, M. Sanquer, *et al.*, A cmos silicon spin qubit, *Nature communications* **7**, 13575 (2016).
- [38] N. W. Hendrickx, W. I. Lawrie, M. Russ, F. van Riggen, S. L. de Snoo, R. N. Schouten, A. Sammak, G. Scappucci, and M. Veldhorst, A four-qubit germanium quantum processor, *Nature* **591**, 580 (2021).
- [39] C. X. Yu, S. Zihlmann, J. C. Abadillo-Uriel, V. P. Michal, N. Rambal, H. Niebojewski, T. Bedecarrats, M. Vinet, É. Dumur, M. Filippone, *et al.*, Strong coupling between a photon and a hole spin in silicon, *Nature Nanotechnology* **18**, 741 (2023).
- [40] F. De Palma, F. Oppliger, W. Jang, S. Bosco, M. Janík, S. Calcaterra, G. Katsaros, G. Isella, D. Loss, and P. Scarlino, Strong hole-photon coupling in planar ge for probing charge degree and strongly correlated states, *Nature Communications* **15**, 10177 (2024).
- [41] M. Janík, K. Roux, C. B. Espinosa, O. Sagi, A. Baghdadi, T. Adletzberger, S. Calcaterra, M. Botifoll, A. G. Manjón, J. Arbiol, *et al.*, Strong charge-photon coupling in planar germanium enabled by granular aluminium superconductors, arXiv preprint arXiv:2407.03079 10.48550/arXiv.2407.03079 (2024).
- [42] V. Michal, J. Abadillo-Uriel, S. Zihlmann, R. Maurand, Y.-M. Niquet, and M. Filippone, Tunable hole spin-photon interaction based on g-matrix modulation, *Physical Review B* **107**, L041303 (2023).
- [43] S. Bosco, P. Scarlino, J. Klinovaja, and D. Loss, Fully tunable longitudinal spin-photon interactions in si and

- ge quantum dots, *Physical Review Letters* **129**, 066801 (2022).
- [44] A. Tosato, V. Levajac, J.-Y. Wang, C. J. Boor, F. Borsoi, M. Botifoll, C. N. Borja, S. Martí-Sánchez, J. Arbiol, A. Sammak, M. Veldhorst, and G. Scappucci, Hard superconducting gap in germanium, *Communications Materials* **4**, 23 (2023).
- [45] O. Sagi, A. Crippa, M. Valentini, M. Janik, L. Baghumyan, G. Fabris, L. Kapoor, F. Hassani, J. Fink, S. Calcaterra, D. Chrastina, G. Isella, and G. Katsaros, A gate tunable transmon qubit in planar ge, *Nature Communications* **15**, 6400 (2024).
- [46] E. Kiyooka, C. Tangchingchai, L. Noiroto, A. Leblanc, B. Brun, S. Zihlmann, R. Maurand, V. Schmitt, E. Dumur, J.-M. Hartmann, F. Lefloch, and S. De Franceschi, Gatemon qubit on a germanium quantum-well heterostructure, *Nano Letters* **10.1021/acs.nanolett.4c05539** (2024).
- [47] M. Valentini, O. Sagi, L. Baghumyan, T. de Gijzel, J. Jung, S. Calcaterra, A. Ballabio, J. Aguilera Servin, K. Aggarwal, M. Janik, T. Adletzberger, R. Seoane Souto, M. Leijnse, J. Danon, C. Schrade, E. Bakkers, D. Chrastina, G. Isella, and G. Katsaros, Parity-conserving cooper-pair transport and ideal superconducting diode in planar germanium, *Nature Communications* **15**, 169 (2024).
- [48] A. Leblanc, C. Tangchingchai, Z. S. Momtaz, E. Kiyooka, J.-M. Hartmann, F. Gustavo, J.-L. Thomassin, B. Brun, V. Schmitt, S. Zihlmann, *et al.*, Gate and flux tunable $\sin(2\varphi)$ josephson element in proximitized junctions, *arXiv preprint arXiv:2405.14695* (2024).
- [49] M. Hinderling, S. C. ten Kate, M. Coraiola, D. Haxell, M. Stiefel, M. Mergenthaler, S. Paredes, S. Bedell, D. Sabonis, and F. Nichele, Direct microwave spectroscopy of andreev bound states in planar Ge josephson junctions, *PRX Quantum* **5**, 030357 (2024).
- [50] L. Lakic, W. I. Lawrie, D. van Driel, L. E. Stehouwer, M. Veldhorst, G. Scappucci, F. Kuemmeth, and A. Chatterjee, A proximitized quantum dot in germanium, *arXiv preprint arXiv:2405.02013* (2024).
- [51] M. Luethi, K. Laubscher, S. Bosco, D. Loss, and J. Klinovaja, Planar josephson junctions in germanium: Effect of cubic spin-orbit interaction, *Phys. Rev. B* **107**, 035435 (2023).
- [52] K. Laubscher, J. D. Sau, and S. Das Sarma, Germanium-based hybrid semiconductor-superconductor topological quantum computing platforms: Disorder effects, *Physical Review B* **110**, 155431 (2024).
- [53] C. Adelsberger, H. F. Legg, D. Loss, and J. Klinovaja, Microscopic analysis of proximity-induced superconductivity and metallization effects in superconductor-germanium hole nanowires, *Physical Review B* **108**, 155433 (2023).
- [54] A. Moghaddam, T. Kernreiter, M. Governale, and U. Zülicke, Exporting superconductivity across the gap: Proximity effect for semiconductor valence-band states due to contact with a simple-metal superconductor, *Physical Review B* **89**, 184507 (2014).
- [55] D. Phan, J. Senior, A. Ghazaryan, M. Hatefipour, W. M. Strickland, J. Shabani, M. Serbyn, and A. P. Higginbotham, Detecting induced $p \pm ip$ pairing at the al-inas interface with a quantum microwave circuit, *Phys. Rev. Lett.* **128**, 107701 (2022).
- [56] Z. Zhu, M. Papaj, X.-A. Nie, H.-K. Xu, Y.-S. Gu, X. Yang, D. Guan, S. Wang, Y. Li, C. Liu, J. Luo, Z.-A. Xu, H. Zheng, L. Fu, and J.-F. Jia, Discovery of segmented fermi surface induced by cooper pair momentum, *Science* **374**, 1381 (2021).
- [57] N. F. Q. Yuan and L. Fu, Zeeman-induced gapless superconductivity with a partial fermi surface, *Phys. Rev. B* **97**, 115139 (2018).
- [58] S. S. Babkin, A. P. Higginbotham, and M. Serbyn, Proximity-induced gapless superconductivity in two-dimensional Rashba semiconductor in magnetic field, *SciPost Phys.* **16**, 115 (2024).
- [59] The terms 'heavy hole' and 'light hole' refer to their respectively large and small effective masses for the motion in the growth direction. However, these effective masses are reversed in the in-plane motion [24]. The names HH (LH) usually refer to their z component of angular momentum $m = \pm 3/2$ ($\pm 1/2$).
- [60] G. Scappucci, C. Kloeffel, F. A. Zwanenburg, D. Loss, M. Myronov, J.-J. Zhang, S. De Franceschi, G. Katsaros, and M. Veldhorst, The germanium quantum information route, *Nature Reviews Materials* **6**, 926 (2021).
- [61] Other materials, such as Si, have a much smaller split-off energy splitting and a 6KP theory is more adequate for their description.
- [62] G. L. Bir and G. E. Pikus, Symmetry and strain-induced effects in semiconductors, (No Title) (1974).
- [63] Z. wang, E. Marcellina, A. R. Hamilton, J. H. Cullen, S. Rogge, J. Salfi, and D. Culcer, Optimal operation points for ultrafast, highly coherent ge hole spin-orbit qubits, *npj Quantum Information* **7**, 10.1038/s41534-021-00386-2 (2021).
- [64] D. Futterer, M. Governale, U. Zülicke, and J. König, Band-mixing-mediated andreev reflection of semiconductor holes, *Physical Review B—Condensed Matter and Materials Physics* **84**, 104526 (2011).
- [65] E. Ivchenko, A. Y. Kaminski, and U. Rössler, Heavy-light hole mixing at zinc-blende (001) interfaces under normal incidence, *Physical Review B* **54**, 5852 (1996).
- [66] S. Babkin, B. Joecker, K. Flensberg, M. Serbyn, and J. Danon, Superconducting proximity effect in two-dimensional hole gases, *arXiv preprint arXiv:2412.04084* 10.48550/arXiv.2412.04084 (2024).
- [67] J. D. Sau, R. M. Lutchyn, S. Tewari, and S. Das Sarma, Generic new platform for topological quantum computation using semiconductor heterostructures, *Phys. Rev. Lett.* **104**, 040502 (2010).
- [68] J. Alicea, Majorana fermions in a tunable semiconductor device, *Physical Review B—Condensed Matter and Materials Physics* **81**, 125318 (2010).
- [69] R. M. Lutchyn, J. D. Sau, and S. Das Sarma, Majorana fermions and a topological phase transition in semiconductor-superconductor heterostructures, *Physical review letters* **105**, 077001 (2010).
- [70] Y. Oreg, G. Refael, and F. von Oppen, Helical liquids and majorana bound states in quantum wires, *Phys. Rev. Lett.* **105**, 177002 (2010).
- [71] N. Ares, V. N. Golovach, G. Katsaros, M. Stoffel, F. Fournel, L. I. Glazman, O. G. Schmidt, and S. De Franceschi, Nature of tunable hole g factors in quantum dots, *Physical review letters* **110**, 046602 (2013).
- [72] D. Paul, 8-band $k \cdot p$ modelling of mid-infrared intersubband absorption in ge quantum wells, *Journal of Applied Physics* **120**, 10.1063/1.4959259 (2016).